A Model of Energy and Spectral Shape for the Internal Gravity Wave Field in the Deep Sea: The Parametric IDEMIX Model

DIRK OLBERS,[a] FRIEDERIKE POLLMANN,[b] ANKITKUMAR PATEL,[b] AND CARSTEN EDEN[b]

[a] *Alfred Wegener Institute for Polar and Marine Research, and MARUM–Center for Marine Environmental Sciences, Universität Bremen, Germany*
[b] *Institut für Meereskunde, Universität Hamburg, Germany*

ABSTRACT: The spectral description of the energy of oceanic internal gravity waves is generally represented by the Garrett–Munk (GM) model, a function with a power-law decrease of spectral energy in wavenumber–frequency space. Besides the slopes of these power laws, the spectrum is expressed as a function of energy and a bandwidth parameter that fixes the range of vertical modes excited in the respective state. Whereas concepts have been developed and agreed upon of what processes feed the wave spectrum and what dissipates energy, there is no explanation of what shapes the spectral distribution, i.e., how the power laws come about and what sets the bandwidth. The present study develops a parametric spectral model of energy and bandwidth from the basic underlying energy balance in terms of forcing, propagation, refraction, spectral transfer, and dissipation. The model is an extension of the IDEMIX (Internal Wave Dissipation, Energy and Mixing) models where bandwidth was taken as a constant parameter. The current version of the model is restricted to single-column mode and the slopes of the spectral power laws are fixed. A coupled system of predictive equations for energy and bandwidth (for up- and downward propagating waves) results. The equations imply that bandwidth relates to energy by a power law with an exponent given by the dynamical parameters. It agrees favorably with energy, bandwidth, and slope data from previously published fits of the GM model to Argo float observations. Numerical solutions of the coupled energy–bandwidth model in stand-alone modus are presented.

KEYWORDS: Energy transport; Inertia-gravity waves; Internal waves; Mixing; Nonlinear models

1. Introduction

Half a century ago, Christopher Garrett and Walter Munk provided the first unified picture of the internal wave field in the ocean by synthesizing a model [later dubbed the Garrett–Munk (GM) model] of the complete wavenumber–frequency spectrum of the wave motion on the basis of linear theory and the available observations (Garrett and Munk 1972). This model (and its extensions) is believed to reflect the spectral features of the internal wave climate in the deep ocean and to possess a certain global validity. Most data obtained later were in good agreement with the model or could be incorporated by modifications, the most severe was the step from the top-hat wavenumber spectrum (GM72) to a sloping one (GM75 and GM76) (Garrett and Munk 1975; Cairns and Williams 1976; Munk 1981; Levine 2002). In 1973, the experiment IWEX (Internal Wave Experiment) was performed in the Sargasso Sea to test the GM model. IWEX results were found in good agreement with GM (Müller et al. 1978), although small but significant deviations were revealed, in particular a vertical asymmetry of wave energies at low frequencies.

The GM spectrum is based on various types of measurements from current meter and thermistors (as a proxy of the vertical displacement). It represents within a factor of about 3 most internal wave properties observed in the World Ocean: the spectral form in wavenumber–frequency space, the spatial coherence of the wave field, and the rms velocities and vertical displacements, but also the vertical dependence of these quantities. Energy is found mainly at low frequencies and large vertical scales while the shear spectrum is concentrated in small vertical scales. Larger deviations from GM are found in singular places such as in the vicinity of extreme topographic features (seamounts, canyons; see, e.g., Eriksen 1982). Moreover, the GM spectrum does not adequately represent the spectral peaks at the inertial frequency and energy at the tidal frequencies are ignored entirely. These peaks have a high variability in time and space and generally also show a vertical asymmetry between up- and downward propagating waves whereas the GM model is symmetric. Near-inertial waves mostly propagate downward, hinting at a likely generation by the wind (Alford et al. 2016; Olbers et al. 2020a). Likewise, baroclinic tidal constituents of the wave field generally propagate upward from their generation site at deep-sea topography (see, e.g., Bell 1975; Garrett and Kunze 2007). In regions under the direct influence of such forcing processes or complicated topography, the internal wave spectrum is hence expected to deviate from the GM model. Outside of these regions, however, and after the wave field has lost the imprint of specific forcing features by interactions with surrounding features or triad wave–wave interactions, the GM model is considered a good (if somewhat smoothed) representation of the ocean's internal wave field (Olbers 1983; Müller et al. 1986).

The GM model is therefore widely used as a reference for spectral features of the ocean's internal wave field. The parameters of the model spectrum, which are energy level, spectral slopes, and bandwidth, are expected to depart from the model constants depending on the local conditions. Regional

---

deviations are documented by Polzin and Lvov (2011), who fitted the GM model to datasets from various locations, and the global the analysis of Pollmann (2020) based on Argo float profiles (Riser et al. 2016) and of Le Boyer and Alford (2021) based on moored velocity records, open a view on the broad geographic variability of these parameters.

Despite the widespread use of the GM model in combination with observations and theoretical concepts, only little progress has been made over the past 50 years to explain the spectral form of the spectrum. The overall GM energy level can be adjusted in most studies to a good agreement with forcing and dissipation scenarios; see, e.g., the discussions in Munk (1981), Olbers (1983, 1986), and Polzin and Lvov (2011). On the other hand, the shape of the spectrum, determined by the slopes in wavenumber–frequency space and the bandwidth of excited (equivalent) vertical modes, has no explanation so far in terms of the wave field's dynamics. Both dominant forcing mechanisms, by wind and by tidal conversion, inject for the most part low modes. The spreading of baroclinic tidal energy in low modes over the spectral range of wavenumbers and frequencies by wave–wave interactions has a complicated transfer pattern and is fairly weak (Olbers et al. 2020b), not immediately leading to the continuous -2 slope in wavenumber–frequency space that the GM model predicts. Further nonlinear transfers with specific properties are necessary but have not been pinned down. It is also unknown how in detail wind-forced waves would spread their energy over the range of the GM continuum. The number of excited modes is usually measured by the roll-off mode number or wavenumber, $j_\star$ or $m_\star$, of the spectral shape function. The observed values of this quantity vary substantially: Polzin and Lvov (2011) report fits to the kinetic energy spectra at various locations, producing roll-offs $j_\star$ ranging from 3 to 20, with lower-amplitude frequency spectra being characterized by larger values of $j_\star$. An understanding of this behavior is absent. A dynamical concept of how the GM roll-off (or bandwidth) is established in terms of forcing, interactions, and dissipation does not exist. It is the topic of the present study.

We develop a dynamical predictive model for the energy level and the modal bandwidth (or roll-off parameter) from the basic radiative energy balance of the wave field, which includes—besides wave forcing at top and bottom of the ocean—propagation, refraction, nonlinear interactions, and dissipation in a wave field with vertical asymmetry. As such, the model is an extension of the IDEMIX (Internal Wave Dissipation, Energy and Mixing) concept, starting with Olbers and Eden (2013) and put forward in various papers by the authors. The energy–bandwidth model is reduced to the simplest setting in the present study: a horizontally homogeneous ocean without mean flow. The basic kinematic and dynamic concepts of such setting are introduced in section 2 and the essential mathematics of the GM class of spectra in section 3. The coupled energy–bandwidth model is derived by a parametric technique first introduced by Hasselmann et al. (1973, 1976) in the context of surface gravity waves. Its specific application to the internal wave problem is described in section 4. In section 5 a fundamental relation between bandwidth and energy is derived. It includes a confirmation of the model results by the data of the

GM fit to Argo observations by Pollmann (2020). Numerical solutions of the model equations are discussed in section 6. Finally, a summary section concludes the study's approach and results.

2. Kinematics and dynamics of small-scale internal waves

In the present study we assume that the oceanic internal waves are essentially linear disturbances of the wave-carrying medium: once they are generated they propagate almost freely along their rays, slowly changing by coupling to their supporting background and nonlinear effects, thereby slowly losing attributes acquired during their particular generation process. Strongly nonlinear effects such as breaking occur only as very localized events in space and time. The waves should have small scales such that a WKBJ approach may be used for spatial scales [meaning essentially that the vertical wavelength should be small compared the scales on which the Brunt–Väisälä frequency $N(z)$ varies in the vertical] and for the temporal variations of the wave amplitudes (they should vary only little over the wave period). In a realistic geophysical situation, the wave field can described by a superposition of a great number of such wave packets, each localized in physical space and having a dominant wavevector, frequency, and amplitude, which slowly change as a consequence of propagation, refraction, reflection, and interactions. Under such conditions the spectral distribution of wave energy is the central property to be determined by observations and explained by dynamical considerations. The aim is thus to acquire knowledge of the energy power spectrum $\mathcal{E}(\mathbf{K}, \mathbf{X}, t)$, which is the density of energy in wavenumber space $\mathbf{K} = (\mathbf{k}, m)$, appropriate at spatial position $\mathbf{X} = (\mathbf{x}, z)$ and time t.

The energetics of a random wave field with the above properties are usually presented by a radiation balance equation (Hasselmann 1968)

$$\partial_t \mathcal{A} + \nabla_\mathbf{X} \cdot (\dot{\mathbf{X}} \mathcal{A}) + \nabla_\mathbf{K} \cdot (\dot{\mathbf{K}} \mathcal{A}) = \mathcal{S}/\omega$$
$$= (\mathcal{S}_\text{gen} + \mathcal{S}_\text{ww} + \mathcal{S}_\text{diss})/\omega \quad (1)$$

for the action spectrum $\mathcal{A}(\mathbf{K}, \mathbf{X}, t) = \mathcal{E}(\mathbf{K}, \mathbf{X}, t)/\omega$, where $\omega = \Omega(\mathbf{K}, \mathbf{X})$ is the intrinsic frequency. Here $\mathcal{S}$ is a source of energy where $\mathcal{S}_\text{gen}$ describes the generation of waves by external processes in the water column, $\mathcal{S}_\text{ww}$ represents the energy in the spectrum due to wave–wave interactions (WWI), and $\mathcal{S}_\text{diss}$ stands for dissipation terms which eliminate wave energy. The fluxes of action in physical and wavenumber space (phase space) are determined by the group velocity $\dot{\mathbf{X}} = \partial_\mathbf{K}\Omega$ and refraction rate $\dot{\mathbf{K}} = -\partial_\mathbf{X}\Omega$. We will not work in the Cartesian coordinates of the phase space but use (ω, m, ϕ) for the wavenumber part where ϕ is the angle of horizontal direction of $\mathbf{k}$ and $k = |\mathbf{k}|$ is transformed to ω. Note that ω is now a coordinate but Ω is still the dispersion function, for internal waves given by

$$\Omega(\mathbf{K}, z) = \left[\frac{N(z)^2 k^2 + f^2 m^2}{k^2 + m^2}\right]^{1/2} \quad (2)$$

with a z-dependent Brunt–Väisälä frequency N and constant Coriolis frequency f.

The present study is restricted to horizontal homogeneous conditions, which means that a single-column model will be considered. In that case $\dot{\phi} = 0$ and $\nabla = 0$ (horizontal derivative). We also assume the absence of a mean flow. The energy spectrum $\mathcal{E} = \mathcal{E}(\omega, m, \phi, z, t)$ is then governed by the simplified radiation balance

$$\partial_t \mathcal{E} + \partial_z \dot{z}\mathcal{E} + \partial_m \dot{m}\mathcal{E} = \mathcal{S} \quad (3)$$

and the following ray equations apply,

$$\dot{z} = -\ell(\omega)/m \quad \text{and} \quad \dot{m} = -n(\omega)\frac{dN}{dz}. \quad (4)$$

The expressions contain the frequency functions

$$\ell(\omega) = \frac{(\omega^2 - f^2)(N^2 - \omega^2)}{\omega(N^2 - f^2)} \quad \text{and} \quad n(\omega) = \frac{N}{\omega}\frac{\omega^2 - f^2}{N^2 - f^2}. \quad (5)$$

The vertical wavenumber m thus changes along the ray but the horizontal wavenumber k remains constant. Note that in spite of horizontal homogeneity the waves still propagate horizontally with their associated horizontal group velocity. The vertical group velocity $\dot{z}$ is opposite to the vertical wavenumber m. We will use the notation $\sigma = \pm$ for up- or downward propagating waves, i.e., $\sigma = -\text{sign}(m)$.

The vertical energy flux $\mathcal{F} = \dot{z}\mathcal{E}$ must be specified at the top and bottom boundaries, assuming for simplicity that these are horizontal surfaces. At the surface

$$\mathcal{F}(\omega, m, \phi) + \mathcal{F}(\omega, -m, \phi) = \Phi_{\text{surf}}(\omega, m, \phi) \quad \text{at} \quad z = 0 \quad (6)$$

must hold, and similarly for the bottom with a net flux $\Phi_{\text{bot}}(\omega, m, \phi)$. The condition accounts for reflection, in which a wave with vertical wavenumber m is reflected into one with $-m$, and an energy source $\Phi_{\text{surf}}(\omega, m, \phi)$ by a wave-maker situated at the surface as e.g., wind stress fluctuations, or by tidal conversion at the bottom in case of $\Phi_{\text{bot}}(\omega, m, \phi)$. If horizontal boundaries are considered then reflecting flux conditions must be implemented there as well.

3. GM spectral model

The knowledge about the structure and importance of the oceanic internal wave field is strongly based on experimental evidence of the wave motion. The first attempt to provide a unified picture of the oceanic internal wave field was made by Garrett and Munk (1972), now 50 years ago, who synthesized a model of the complete wavenumber–frequency spectrum (GM model) of the motion in the deep ocean on the basis of linear theory and the available observations by horizontally or vertically separated moored instruments or dropped sondes. The model underwent a few and relatively modest modifications (Garrett and Munk 1975; Cairns and Williams 1976; Müller et al. 1978; Munk 1981; Levine 2002) and has been widely used to represent the deep ocean's internal wave climate ever since. In a broad brush view the GM spectrum,

as density of (ω, m), is characterized by a ω^{-2} decay of energy power in frequency space with a minor peak at $\omega = f$ (generally underrepresenting the actual near-inertial peak at most sites) and a m^{-2} decay in vertical wavenumber space with a roll-off at wavenumber $m = m_\star$ to a plateau at low wavenumbers. GM is horizontally isotropic and of the factorized form shown below with a vertically symmetric wavenumber spectrum. This model version is referred to as GM76.

In the present study we consider the GM spectrum in the generalized form

$$\mathcal{E}_{\text{GM}}(\omega, m, \phi, z) = E_{\text{GM}}(z)\frac{1}{2\pi}A(m)B(\omega) \quad \text{with}$$

$$A(m) = \frac{1}{2}\frac{\tilde{A}(|m|/m_\star, s)}{m_\star} \quad (7)$$

having a total energy $E_{\text{GM}}(z)$ at depth z and depending on the shape parameters $m_\star$, a wavenumber scale, and a spectral slope s of the wavenumber distribution. The shape function $\tilde{A}(\lambda, s)$ and $B(\omega)$ are normalized to one,

$$\int_0^\infty \tilde{A}(\lambda, s)d\lambda = 1 \quad \text{and} \quad \int_f^N B(\omega)d\omega = 1, \quad (8)$$

and the factors $1/2\pi$ and $1/2$ in Eq. (7) then derive from horizontal isotropy and vertical symmetry. The vertical wavenumber spectrum $A(m)$ is thus defined as two-sided (its integral taken only over positive wavenumbers is unity).

For the frequency spreading function $B(\omega)$ we consider the original GM form

$$B(\omega) = n_B \frac{|f|}{\omega(\omega^2 - f^2)^{1/2}} \quad \text{for} \quad f \leq \omega \leq N(z). \quad (9)$$

The Coriolis frequency is here implemented for clarity as modulus; the signs of absolute value, however, will generally be omitted in the following. The normalization n_B is $2/\pi$ for $N/f \gg 1$, its general form is given in appendix A. The wavenumber distribution of the GM spectral model is given by the generalized form

$$\tilde{A}(\lambda, s) = n_A(s)\frac{1}{1 + \lambda^s} \quad \text{for} \quad \lambda_\ell \leq \lambda \leq \lambda_c, \quad (10)$$

where $\lambda = |m|/m_\star$, specifying now s as slope[1] at high wavenumbers. For $s = 2$ the wavenumber shape is that of the standard model GM76 (Cairns and Williams 1976). Some physical quantities, such as vertical shear or vertical energy flux, need a low (at $\lambda = \lambda_\ell \ll 1$) or a high (at $\lambda = \lambda_c \gg 1$) wavenumber cutoff such that $\tilde{A}(\lambda) = 0$ for $0 \leq \lambda \leq \lambda_\ell = m_\ell/m_\star$ and $\lambda \geq \lambda_c = m_c/m_\star$. In this case the normalization is $n_A(s = 2) = (\arctan\lambda_c - \arctan\lambda_\ell)^{-1}$. The normalization $n_A(s)$ for a general slope is given appendix A.

---

[1] Note that we use positive values for slope. The actual slope of the spectrum is $-s$.

For the standard GM76 model the parameter values are $E_{GM} = \times 10^{-3}$ m^2 s^{-2}, $m_\star = 0.01$ m^{-1}, and $s = 2$, to be used for simple order of magnitude calculations. Depending on when, where, and how the ocean's internal wave field is observed, departures from the standard GM76 parameters are to be expected (e.g., Polzin and Lvov 2011; Le Boyer and Alford 2021). Pollmann (2020) fitted the GM spectral model with parameters E, $m_\star$, and s to 12 years' worth of Argo data. Contrary to single research cruises or dedicated observation programs, the Argo database offers a nearly global coverage, is not biased toward certain areas or seasons, and, with more than 20 years of operation, provides a sufficiently long observation period to characterize the background internal wave climate of the ocean that the GM model is meant to represent (rather than a snapshot).

Argo floats collect temperature, salinity, and pressure information at a vertical resolution of a few meters. Following the first steps of the fine-structure method (Gregg 1989; Kunze et al. 2006; Whalen et al. 2012; Polzin et al. 2014), vertical wavenumber spectra of strain can be obtained. The polarization relations link spectra of strain and energy

$$\mathcal{E}(\omega, m) = \frac{\omega^2}{m^2} \frac{N^2 - f^2}{\omega^2 - f^2} S_{\xi_z}(\omega, m), \qquad (11)$$

where $S_{\xi_z}(\omega, m)$ denotes the strain spectrum. By integrating this relation over all frequencies and assuming that the frequency-dependent part of $\mathcal{E}(\omega, m)$ follows exactly the GM model's form Eq. (9), the Argo-derived strain spectra $S_{\xi_z}(m)$ can be used to estimate the parameters m_* and s of the GM vertical wavenumber energy spectrum $A(m)$ (Pollmann et al. 2017; Pollmann 2020). The details of the method as well as the fitting procedure are described in Pollmann (2020).

It is important to remember that owing to the relatively coarse resolution of the fine-structure observations, the resultant energy levels, dissipation rates, or spectral parameter fits have a higher uncertainty than, e.g., those estimated from microstructure observations. Such high-resolution observations are, however, not available in such numbers that allow a nearly global mapping of internal wave characteristics, which makes the fine-structure method applied to the Argo database (with the above caveat in mind) an invaluable tool to outline the geographic variability of the GM model parameters and as such a central benchmark for IDEMIX modeling.

In the upper ocean, the internal wave energy levels vary by about two orders of magnitude from pole to equator, with the GM76 reference value of $E_{GM} = 3 \times 10^{-3}$ m^2 s^{-2} mainly found at latitudes equatorward of 60° or 40° in the northern and southern hemispheres, respectively (Fig. 1a). There is a similar variability in wavenumber scale $m_\star$ (Fig. 1b). The spectral slope variation, on the other hand, is rather weak and ranges only from 1.6 to 2.4 (Fig. 1c). GM76 reference values of $m_\star = 0.01$ m^{-1} and $s = 2$ are found mainly in the Southern Ocean and in the vicinity of maxima in the northwest Pacific, the North Atlantic, and the tropical Indian Ocean. Figure 2 shows the relation between two of the three parameters while keeping the third fixed. The curve describing their interdependence is either a power law [$\log(m_\star)$ versus $\log(E)$], a

curved line [$\log(m_\star)$ versus s], or a point cloud [$\log(E)$ versus s]. The first of these relations, the decrease of the roll-off $m_\star$ with increasing energy, was reported by Polzin and Lvov (2011), using a collection of kinetic energy spectra at various locations. An understanding of such correlation between $m_\star$ and E, however, remained absent. The relevance of the parameter correlations will become clear in the following sections.

4. A model of spectral energy and shape

To extend the energy equations developed in the IDEMIX models (Olbers and Eden 2013; Eden and Olbers 2014), we develop a concept for computing the spectral bandwidth for internal gravity waves from a prognostic equation, derived from a general definition of bandwidth as a functional of the local spectrum, and the wave radiation balance. The analytical derivations are along the IDEMIX framework, but here we exploit a general parametric approach. The approach is utilized to derive a fully coupled model for energy and bandwidth of the GM class of spectra. To simplify the problem we restrict the analysis to single column physics without mean flow.

Let $\mathcal{E}(\omega, m, \phi, z, t)$ be the actual spectrum and assume that we have at any position and time a good approximation by a parametric form $\hat{\mathcal{E}}(\omega, m, \phi; a_1, a_2, ..., a_n)$, characterized by free parameters $a_1, a_2, ..., a_n$, which are functions of (z, t). The spectrum $\hat{\mathcal{E}}$ is here the GM class of spectral forms, described in the preceding section, and, e.g., a_1 would be the energy of upward propagating waves in the wave field and a_2 that of the downward propagating waves, other parameters may be bandwidth, slope, etc. Clearly, the functional $\hat{\mathcal{E}}(\omega, m, \phi; a_1, a_2, ..., a_n)$ can only represent a subclass of possible spectra and the projection on this subclass can only be meaningful if the evolution of the true spectrum $\mathcal{E}(\omega, m, \phi, z, t)$ stays close to this subclass during its evolution. We now follow Hasselmann et al. (1973, 1976) to construct equations of motion for the spectral parameters by a well-defined projection of the radiation balance.

a. Hasselmann's parametric approach

To approximate $\mathcal{E}(\omega, m, \phi, z, t)$ by a member of $\hat{\mathcal{E}}(\omega, m, \phi; a_1, a_2, ..., a_n)$ an algorithm Φ_i must be introduced for each parameter a_i that defines a best-fit $a_i = \Phi_i(\mathcal{E})$. A variation $\delta\mathcal{E}$ (e.g., in time) of $\mathcal{E}$ leads to a variation of the parameter a_i,

$$\delta a_i = \Phi'_i(\delta\mathcal{E}) = \Phi_i(\mathcal{E} + \delta\mathcal{E}) - \Phi_i(\mathcal{E}), \qquad (12)$$

where the functional derivative Φ'_i is by construction a linear operator. Consider an example: $a_1(z, t) = \Phi_1(\mathcal{E}) = \int_{-\infty}^{0} dm \int d\omega \int d\phi \, \mathcal{E}(\omega, m, \phi, z, t)$ is an estimator of the energy of the upward propagating waves. Here, Φ_1 is linear (integration over frequency and wavenumber) and hence Φ'_1 is the same operator as Φ_1. For other parameters this may not hold.

Considering a specific variation of a spectrum from the parametric subclass, $\delta\mathcal{E} = (\partial\hat{\mathcal{E}}/\partial a_j)\delta a_j$ (sum convention is assumed), we find $a_i \Phi'_i(\partial\hat{\mathcal{E}}/\partial a_j)a_j$ so that the relation

$$\Phi'_i(\partial\hat{\mathcal{E}}/\partial a_j) = \delta_{ij} \qquad (13)$$
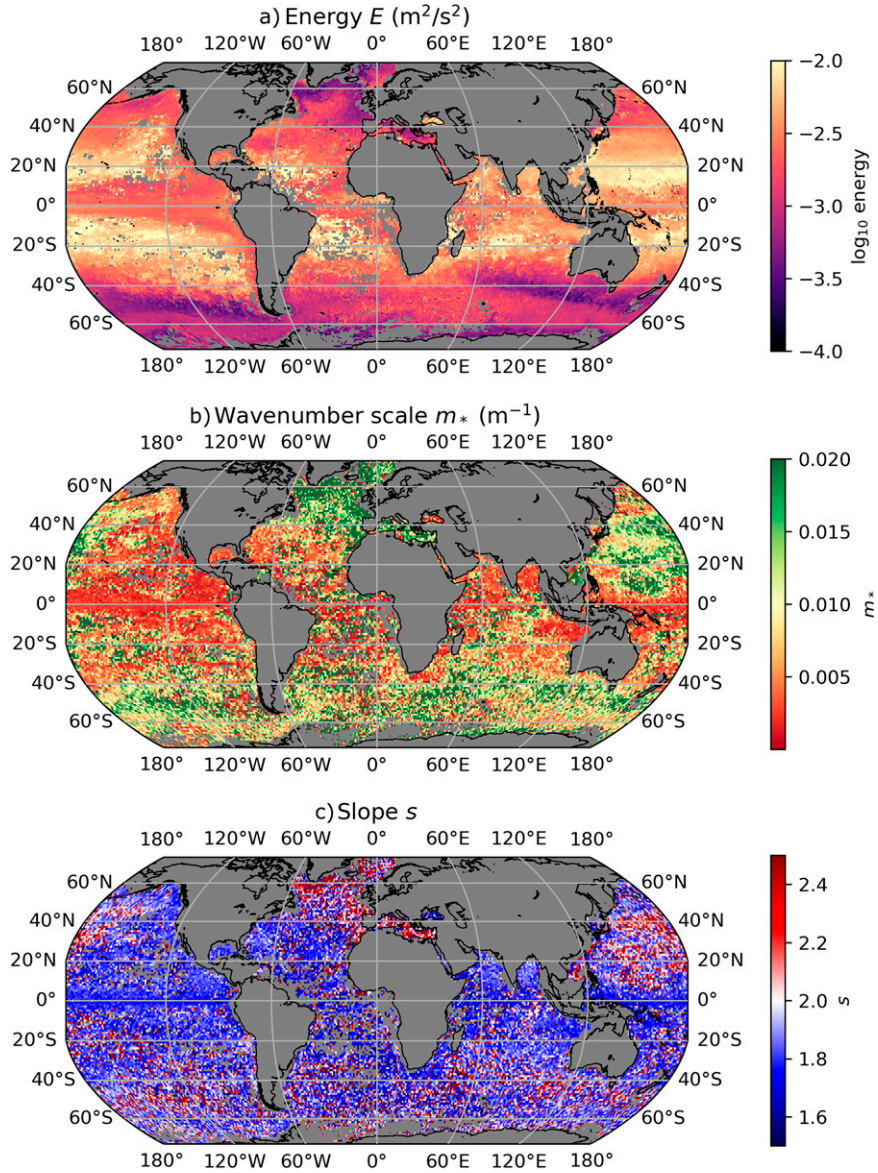
a) Energy E (m²/s²)

b) Wavenumber scale m_* (m⁻¹)

c) Slope s

FIG. 1. Spectral parameters (a) energy level E, (b) wavenumber scale m_*, and (c) slope s as estimated by Pollmann (2020) from Argo float profiles and averaged between 300- and 500-m depth. The processed data are available from Pollmann (2022).

must hold. The term δ_{ij} is the Kronecker tensor. The operator Φ'_i is then used to project the radiation balance on the parameter a_i. For instance, we insert below the parametric spectral form[2] into the single-column version Eq. (3) of the IW energetics,

$$\frac{\partial \hat{\mathcal{E}}}{\partial a_j} \partial_t a_j + \partial_z \dot{z}\hat{\mathcal{E}} + \partial_m \dot{m}\hat{\mathcal{E}} = \hat{\mathcal{S}}, \qquad (14)$$

and apply the projection operator Φ'_i with the orthogonality property Eq. (13), to obtain the rate of change of the parameter a_i,

$$\partial_t a_i + \Phi'_i \partial_z (\dot{z}\hat{\mathcal{E}}) + \Phi'_i (\partial_m \dot{m}\hat{\mathcal{E}}) = \Phi'_i(\hat{\mathcal{S}}). \qquad (15)$$

Note that Φ'_i operates on the (ω, m, ϕ) dependence only, not on the parametric variables of the spectrum and not on the space and time coordinates. For our example a_1, the projection of $\partial_m \dot{m}\hat{\mathcal{E}}$ in Eq. (14) yields zero[3] and we end up with the IDEMIX equations for the single column models, as developed in Olbers and Eden (2013). In the following section, we

---

[2] All hatted variables are parametric.

[3] For spectral models with cutoffs in wavenumber space this does not hold.
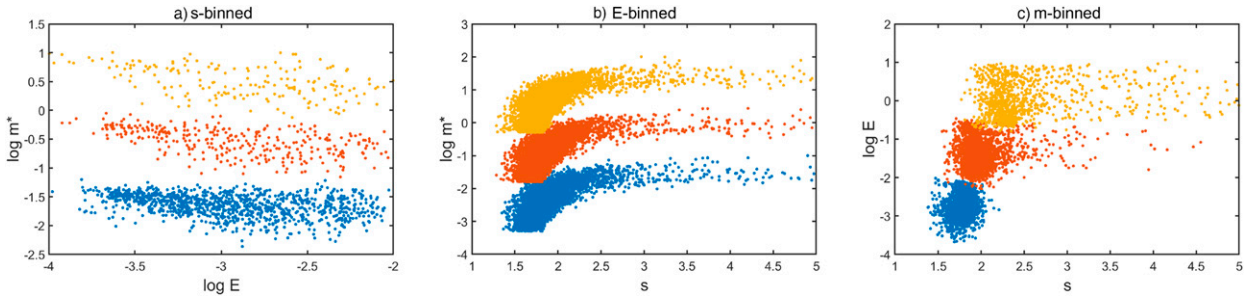
FIG. 2. Scatterplot for data for the depth range 300–500 m: (a) s sliced in bins 2.3–2.5, 2.7–2.9, and 3.1–3.3; (b) E sliced with $\log_{10}(E)$ in bins from -3.0 to -2.8, from -2.9 to -2.7, and from -2.8 to -2.6; (c) m sliced with $\log_{10}(m)$ in bins from -2.6 to -2.5, from -2.0 to -1.9, and from -1.6 to -1.5. Data with red colored dots are displaced by a factor 10, those in yellow by a factor 100 on the respective vertical axis.

generalize this model to include spectral parameters other than energy, and use the parametric approach.

b. The parametric approach applied to the GM class

Our parametric model is an extended form of the GM spectrum presented in section 3. We use

$$\hat{\mathcal{E}}(\omega, \mp|m|, \phi, z, t) = \hat{A}^{\pm}(m, \phi)B(\omega)$$
$$= \epsilon^{\pm} \frac{\tilde{A}(|m|/m_{\star}^{\pm}, s^{\pm})}{m_{\star}^{\pm}} B(\omega) S(\phi), \quad (16)$$

with $\lambda = |m|/m_{\star}$. In Eq. (16), $B(\omega)$ is the usual normalized frequency shape function Eq. (9) of the GM class and $\hat{A}^{\pm}(m; \phi)$ is the wavenumber spectrum with the function $\tilde{A}$ given by Eq. (10). The difference to the conventional GM model is that the parameters $\epsilon^{\pm}$, $m_{\star}^{\pm}$, and $s^{\pm}$ take different values for the wavenumber branches $m < 0$ (upward propagating waves) and $m > 0$ (downward propagating waves). In the parametric model there are two scale parameters $\epsilon^{\pm}$ and there are four shape parameters $m_{\star}^{\pm}$ and $s^{\pm}$. Note that $\tilde{A}(|m|/m_{\star}^{\pm}, s^{\pm})/m_{\star}^{\pm}$ describes the spectrum on both sides with the same shape function but different bandwidths and slopes. It is normalized by integrating over the wavenumber half-space.

Although the actual spectrum will certainly go beyond the limits λ_{ℓ} and λ_c in Eq. (10) we regard these ranges as not occupied by internal waves (in the same sense that fluctuations with frequencies outside $[f, N(z)]$ are not internal waves). In general, we assume $\lambda_{\ell} \ll 1 \ll \lambda_c$. We must distinguish in the expression of Eq. (16) between "parameters" and "coefficients," which both shape the appearance of the spectrum. The first specie, the $a_j, j = 1, \ldots, n$, form the fundament of the parametric model; they have a (z, t) dependence. The second specie, basically the Coriolis frequency f, the Brunt–Väisälä frequency N, and the cut-offs λ_{ℓ} and λ_c, are coefficients with fixed values. We refer to the so described spectral function as GM class.

In the present study we simplify and assume that the slopes $s^{\pm}$ are constant, in most applications they are even identical in the up–down compartments (but not fixed to 2 as in GM76). Predictive slope equations will be considered in a future study. The aim of our project is to develop parametric model

equations for ϵ and $m_{\star}$, in the present study for zero mean flow. In that case we can choose $S(\phi) = 1/2\pi$ isotropic and the parametric spectrum Eq. (16) may be integrated over ϕ and similarly the radiation balance Eq. (3). In the following analysis we thus consider the balance of the actual wavenumber spectrum

$$G(m) = \int d\phi \int d\omega \mathcal{E}(\omega, m, \phi) = \int d\phi A(m, \phi), \quad (17)$$

which is given by

$$\partial_t G - \partial_z \overline{\ell} G/m - \partial_m \overline{n} \frac{dN}{dz} G = \int d\phi \int d\omega \mathcal{S} = \mathcal{Q}. \quad (18)$$

Here $\overline{\ell}$ and $\overline{n}$ are the frequency-averaged coefficients with respect to weighting by $B(\omega)$, they are given in appendix A. The source term $\mathcal{Q}$ derives from $\mathcal{S}$ by the indicated integration. Integrating the parametric spectrum over ϕ and ω yields the parametric form of the wavenumber distribution,

$$\hat{G}(m) = \int d\phi \hat{A}^{\pm}(m, \phi) = \epsilon^{\pm} \frac{\tilde{A}(|m|/m_{\star}^{\pm}, s^{\pm})}{m_{\star}^{\pm}}. \quad (19)$$

1) PROJECTING ON ENERGY

We estimate the compartmental energies by

$$\epsilon^{\pm} = \int^{\pm} dm \, G(m) = \Phi_{\epsilon}^{\pm}(G) \quad (20)$$

with projector

$$\Phi_{\epsilon}^{\prime \pm}(g) = \int^{\pm} dm \, g \quad (21)$$

with $\int^{-} dm = \int_{m_{\ell}}^{m_c} dm$ as integral for downward waves (which have positive wavenumbers) whereas $\int^{+} dm = \int_{-m_c}^{-m_{\ell}} dm$ is for upward waves (which have negative wavenumbers). We insert the model $\hat{G}$ for the actual spectrum A into Eq. (18) and project,

$$\partial_t \epsilon - \partial_z \frac{\overline{\ell}\epsilon}{m_{\star}} \Phi_{\epsilon}^{\prime}(\tilde{A}/m) - \frac{dN}{dz} \frac{\overline{n}\epsilon}{m_{\star}} \Phi_{\epsilon}^{\prime}(\partial_m \tilde{A}) = \Phi_{\epsilon}^{\prime}(\hat{\mathcal{Q}}) = \Theta. \quad (22)$$

Here Θ is the projection of the model source $\hat{Q}$. The respective parameters ϵ and $m_\star$ carry their $\pm$ (up–down compartments) indices, which are here and in most of the following relations omitted. We detail all projections in Eq. (22) in appendix B.

2) PROJECTING ON BANDWIDTH

Though an estimator of the wavenumber scale $m_\star$ can be set up, we prefer a slight detour, mainly because an equation directly predicting $m_\star$ also needs physically motivated boundary conditions, which are not at all intuitive. We thus consider the parameter

$$a^\pm = \int^\pm dm \, G^2(m) = \Phi_a^\pm(G), \qquad (23)$$

which turns out to be $a^\pm = (\epsilon^\pm)^2/[\eta(s)m_\star^\pm]$ for the GM class. Here $\eta(s)$ is a function of slope, given in appendix A. We will refer to the parameter a as "squared energy." Once energy and squared energy are predicted the wavenumber scale can be simply diagnosed.

The projection operator associated with this parameter is

$$\Phi_a'^\pm(g) = 2\int^\pm dm \, \hat{G}g = 2\frac{\epsilon}{m_\star}\int^\pm dm \, \tilde{A}g. \qquad (24)$$

Projection yields, taking the integrated form Eq. (18) of the balance,

$$\partial_t a - \Phi_a'\left(\partial_z \frac{\overline{\ell}\epsilon}{m_\star}\tilde{A}/m\right) - \frac{dN}{dz}\frac{\overline{n}\epsilon}{m_\star}\Phi_a'(\partial_m\tilde{A}) = \Phi_a'(\hat{Q}) = Y, \qquad (25)$$

and again we detail the evaluation of the projection terms to appendix B.

As a side note we mention that the parameter $m_\star$ is often referred to as spectral bandwidth of GM. However, such a conflation becomes questionable when variations of the slope are considered: spectra with same $m_\star$ but different s have a greatly differing apparent width. A convenient definition of bandwidth, taking care of such dependencies, is the bandwidth functional

$$m_b = \frac{\left(\int dm \, G\right)^2}{\int dm \, G^2}. \qquad (26)$$

It has the property that bandwidth multiplied by a spectrally averaged energy spectrum yields the total energy, i.e., m_b times the integral of the energy spectrum, weighted by $G/\int G$, equals $\int G$. Such an estimator is of advantage where quadratic and higher moments of the spectrum do not exist. It turns out that $m_b = \epsilon^2/a = \eta m_\star$. Differences are subtle, and we continue to call $m_\star$ bandwidth.

3) PROJECTION OF SOURCES AND SINKS

The source terms Θ and Y on the right-hand sides of Eqs. (22) and (25) must still be derived in parametric form. In the present

study we ignore interior (in the ocean water column) sources and sinks of energy other than those due to WWI and dissipation such that $Q = Q_{ww} + Q_{diss}$. A parametric model of these terms is required in order to perform the projections. We base a model on the findings in Eden et al. (2019) for the parameter dependence of the WWI source term,

$$\hat{Q}_{ww}(|m|, \phi) = \frac{1}{2\pi}\frac{fE^2M_\star^2}{N^2(s-1)^3}\psi_w(|m|) = \frac{1}{2\pi}\frac{E}{\tau_E}\psi_w(|m|). \qquad (27)$$

Here $\psi_w(|m|)$ is the shape function of the transfer in m space. The time scale

$$\tau_E(E, s, N) = \frac{N^2(s-1)^3}{fEm_\star^2} \qquad (28)$$

of nonlinear WWI enters this expression (for the standard GM values it is about 15 days). We use total (up plus down) energy $E = \epsilon^+ + \epsilon^-$ and energy asymmetry $\Delta = \epsilon^+ - \epsilon^-$, as before in IDEMIX publications.[4]

For an asymmetric spectrum, as assumed in the parametric model, the scaling of the WWI source term requires an asymmetric form of Eq. (27) which is unknown. A plausible extrapolation is

$$\hat{Q}_{ww}(m, \phi) = \frac{1}{2\pi}[E\psi_w^s(m) + \Delta\psi_w^a(m)]/\tau_E$$

$$\psi_w^s(m) = \frac{1}{2}[\psi_w(m) + \psi_w(-m)] \quad \text{and}$$

$$\psi_w^a(m) = \frac{1}{2}[\psi_w(m) - \psi_w(-m)]. \qquad (29)$$

We assume the corresponding form for $\hat{Q}_{diss}$ but with a different shape function $\psi_d(m)$. Straightforward application of the parametric projection then leads to

$$\Theta = -\frac{1}{2}(\mu_0 E + \sigma\mu_1\Delta)\frac{1}{\tau_E} \quad \text{and} \quad Y = -\frac{\epsilon}{m_\star}(\mu_2 E + \sigma\mu_3\Delta)\frac{1}{\tau_E} \qquad (30)$$

with coefficients μ_0, μ_1, μ_2 and μ_3 given below.

The coefficient μ_0 derives from the spectrum of dissipation and the associated source term $Q_{diss}(m, \phi)$ is parameterized as the WWI term. For the latter, however, a symmetric form is here sufficient with shape function $\psi_d(m)$ which is only nonzero in the dissipation range $|m| > m_d$. Then

$$\mu_0 = -2\int_{m_d}^\infty \psi_d dm. \qquad (31)$$

The other coefficients are found as integrals of ψ_w,

$$\mu_1 = -2\int_0^\infty \psi_w^a dm, \quad \mu_2 = -2\int_0^\infty \tilde{A}\psi_w^s dm,$$

$$\mu_3 = -2\int_0^\infty \tilde{A}\psi_w^a dm. \qquad (32)$$

---

[4] Note that we have changed the notation for the energy asymmetry Δ from that in previous IDEMIX papers.

Except for the gross structure of $\psi_w(m)$, as found in Olbers (1976) and Eden et al. (2019), we know only little about the shape functions: they should reflect a transfer from low to high wavenumbers and, with the notion that spectral asymmetries should be small, the symmetric part ψ_w^s is much larger than the asymmetric part ψ_w^a. Obviously $\mu_0 > 0$ since dissipation extracts energy at high wavenumbers (ψ_d is negative). Furthermore, we assume $\mu_1 > 0$ such that asymmetric energy Δ is damped by WWI. Also μ_2 is positive because of the weighting of ψ_w^s by decaying $\bar{A}$ in the integral. Note that Eq. (30) leads to a net dissipation $-\mu_0 E/\tau_E$ of total energy E and damping $-\mu_1\Delta/\tau_E$ of energy asymmetry Δ by with the respective time scales τ_E/μ_0 and τ_E/μ_1, and correspondingly for the variables of squared energy.

c. The equations of the coupled model

The balance equations for energy and squared energy, Eqs. (22) and (25) now read

$$\partial_t \epsilon + \sigma \partial_z \left(\frac{\bar{\ell}\gamma_1 n_A \epsilon}{m_\star} \right) + T_\epsilon = -\frac{1}{2}(\mu_0 E + \sigma\mu_1 \Delta)\frac{1}{\tau_E}, \qquad (33)$$

$$\partial_t \frac{\epsilon^2}{\eta m_\star} + \sigma n_A \epsilon \partial_z \left(\frac{\bar{\ell}\gamma_2 n_A \epsilon}{m_\star^2} \right) + T_a = -\frac{\epsilon}{m_\star}(\mu_2 E + \sigma\mu_3 \Delta)\frac{1}{\tau_E}. \qquad (34)$$

Turning point transfers have been introduced:

$$T_\epsilon = -\sigma\frac{dN}{dz}\frac{\bar{n} n_A \epsilon}{m_\star} \quad \text{and} \quad T_a = -\sigma\frac{dN}{dz}\frac{\bar{n} n_A^2 \epsilon^2}{m_\star^2}. \qquad (35)$$

These terms arise by straightforward projection, as explained in appendix B. They are attributed to turning point effects because they represent an exchange of energy between up and down waves due to a varying Brunt–Väisälä frequency. The exchange in the form Eq. (35) is, however, not energy conserving, which turning point physics should obey. To this extent the projection has to be formulated in an upstream form, see appendix B. We use the energy conserving form later in section 6. A number of coefficients have entered the parametric model, all of which are well defined as integrals of the shape functions of the GM class. All coefficients are found in Eqs. (31) and (32) and appendix A.

It is a simple matter to eliminate $\partial_t \epsilon$ between Eqs. (33) and (34) and derive a predictive balance for the bandwidth $m_\star$. It is given in appendix C for later reference. We will not use the bandwidth balance in a predictive way but rather determine $m_\star$ as a diagnostic from the solution of Eqs. (33) and (34).

To complete the parametric equations Eqs. (33) and (34) boundary conditions (BC) must be specified. For any of the up or down version of energies [$\epsilon^\pm$ or $(\epsilon^\pm)^2/m_\star^\pm$] there are conditions to be satisfied at either top $z = 0$ or bottom $z = -h$, which follow from the BC Eq. (6) of the radiation balance. Boundary conditions for energy follow the same rationale as in the previous IDEMIX treatments as in Olbers and Eden (2013) but we repeat it here.

1) BOUNDARY CONDITIONS FOR ENERGY

The flux of ϵ^+ is $J^+ = \bar{\ell}\gamma_1 n_A \epsilon^+/m_\star^+$ and correspondingly for ϵ^- where we have $J^- = -\bar{\ell}\gamma_1 n_A \epsilon^-/m_\star^-$. Hence, $J^+ > 0$ and $J^- < 0$. At the surface J^+ is unrestricted and would transport energy ϵ^+ out of the water column but we require conservation of total energy $\epsilon^+ + \epsilon^-$. As consequence, the flux into the water by J^- must be

$$J^- = -J^+ + F_{\text{surf}} \quad \text{at} \quad z = 0. \qquad (36)$$

The convention is here that $F_{\text{surf}} < 0$ for the net surface flux. We thus diagnose $J^+ = \bar{\ell}\gamma_1 n_A \epsilon^+/m_\star^+$ at the surface and set the downward (inward) J^- accordingly. At the bottom the situation is similar: Here we diagnose the incident $J^- = \bar{\ell}\gamma_1 n_A \epsilon^-/m_\star^-$ at the bottom and put

$$J^+ = -J^- + F_{\text{bot}} \quad \text{at} \quad z = -h \qquad (37)$$

with the convention $F_{\text{bot}} > 0$ for the net bottom flux. In both cases the BCs may be formulated as conditions of the flux $J^+ + J^- = F_{\text{surf}}$ or F_{bot} of total energy at the corresponding boundaries.

2) BOUNDARY CONDITIONS FOR SQUARED ENERGY

What do we learn from this exercise for the BCs to be posed for the squared energy parameter $\epsilon^2/m_\star$? The appropriate expression for the flux is identified from Eq. (34). The flux of $(\epsilon^+)^2/(\eta m_\star^+)$ is $L^+ = \bar{\ell} n_A \gamma_2 (n_A \epsilon^+)^2/(m_\star^+)^2$ and similarly, the flux of $(\epsilon^-)^2/(\eta m_\star^-)$ is $L^- = -\bar{\ell}\gamma_2 (n_A \epsilon^-)^2/(m_\star^-)^2$. And again $L^+ > 0$, $L^- < 0$. But the $L^\pm$ are not independent of the $J^\pm$, in fact we have

$$L^\pm = \pm\zeta(J^\pm)^2 \quad \text{with} \quad \zeta = \gamma_2/(\bar{\ell}\gamma_1^2). \qquad (38)$$

5. The bandwidth–energy relation

We now look for analytical solutions of the parametric model for steady-state conditions. The following approach leads to a relation between bandwidth and energy, which is then used to find solutions for the energy balance.

a. An exact integral

The source terms (WWI and dissipation) in Eqs. (33) and (34) have a similar structure and with the simple and reasonable assumption $\mu_2 = \mu n_A \mu_0$, $\mu_3 = \mu n_A \mu_1$ they may be put into identical form and thus can be eliminated between the two equations. The factor μ should be of order 1 and may depend on s (the common factor n_A simplifies the following equations). The analysis of the Argo data in the next section justifies this setting. Hence, assuming steady state and taking the difference the complicated WWI and dissipation terms cancel and we find

$$\sigma\bar{\ell} n_A^2 \gamma_2 \partial_z \ln\left(\frac{\bar{\ell} n_A \epsilon}{m_\star^2} \right) - 2\sigma\bar{\ell} n_A^2 \gamma_1 \mu\partial_z \ln\left(\frac{\bar{\ell} n_A \epsilon}{m_\star} \right) + \frac{m_\star^2}{\epsilon^2}T_a$$

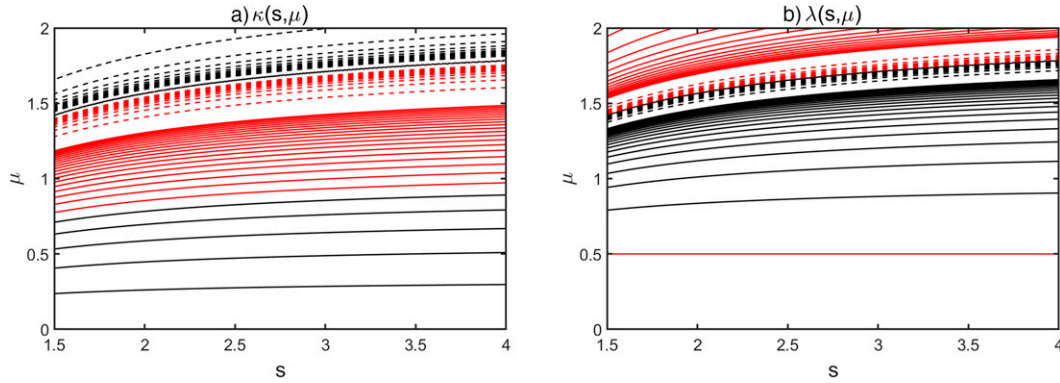$$- 2\mu n_A \frac{m_\star}{\epsilon}T_\epsilon = 0. \qquad (39)$$

FIG. 3. (a) The exponent κ as given in Eq. (44) as function of s and μ. Red contours are for negative values and black for positive. The contour step for full lines is 0.1 and for dashed lines 2. (b) As in (a), but for the exponent λ.

The turning point terms combine to $-\sigma n_A^2(1 - 2\mu)\overline{n}(dN/dz)$ and the equation reduces to

$$\partial_z \ln\left[\left(\frac{\overline{\ell}n_A\epsilon}{m_\star^2}\right)^{\gamma_2}\left(\frac{\overline{\ell}n_A\epsilon}{m_\star}\right)^{-2\mu\gamma_1}\right] = (1 - 2\mu)\frac{\overline{n}}{\overline{\ell}}\frac{dN}{dz}. \quad (40)$$

Surprisingly, the turning point term can be included in the logarithmic flux because

$$\frac{\overline{n}}{\overline{\ell}} = \frac{1}{2}\frac{1}{C}\frac{\partial}{\partial N}C \quad \text{with} \quad C = \int_f^N \frac{\sqrt{\omega^2 - f^2}}{\omega^2}(N^2 - \omega^2)d\omega. \quad (41)$$

The C function is a logarithmic function of N/f and given in appendix A. Finally, we arrive at

$$\partial_z \ln\left[\left(\frac{\overline{\ell}n_A\epsilon}{m_\star^2}\right)^{\gamma_2}\left(\frac{\overline{\ell}n_A\epsilon}{m_\star}\right)^{-2\gamma_1\mu}C^{(2\mu-1)/2}\right] = 0, \quad (42)$$

which is readily integrated,

$$(\overline{\ell}n_A\epsilon)^{\gamma_2 - 2\mu\gamma_1}(m_\star)^{-2\gamma_2 + 2\mu\gamma_1}C^{(2\mu-1)/2} = \text{const}, \quad (43)$$

with a z-independent but dimensioned constant. The roll-off parameter $m_\star$ is related to the energy ϵ by a power law,

$$m_\star = \Gamma(\overline{\ell}n_A\epsilon)^\kappa C^\lambda = \Gamma(\overline{\ell}^\kappa C^\lambda)(n_A\epsilon)^\kappa, \quad (44)$$

with the exponents

$$\kappa = \frac{1}{2}\frac{\gamma_2 - 2\mu\gamma_1}{\gamma_2 - \mu\gamma_1} \quad \text{and} \quad \lambda = \frac{1}{4}\frac{2\mu - 1}{\gamma_2 - \mu\gamma_1}. \quad (45)$$

The constant Γ in Eq. (44) is depth independent but may be dependent on slope. The exponents κ and λ can have either sign, depending on the values of s and μ, as shown in Fig. 3. The contribution of the C term comes from turning point transfers. Note that $m_\star$, ϵ, $\overline{\ell}$, and C are z dependent. In the second relation in Eq. (44) we have separated the dependence of $m_\star$ on ϵ from the z dependence in the Brunt–Väisälä frequency terms $\overline{\ell}$ and C.

Equation (44) is only part of the solution: it must be inserted into the energy balance to find the energy ϵ in terms of forcing and dissipation. To this extent we must get a handle on the constant Γ in Eq. (44), which is not a free coefficient but rather given by BCs. With knowledge of the values of $L^\pm = L_{0,-h}^\pm$ at the boundaries we use Eq. (44) to find

$$\Gamma^2 = \frac{1}{|L|}\frac{\overline{\ell}\gamma_2 n_A^2\epsilon^2}{(\overline{\ell}n_A\epsilon)^{2\kappa}C^{2\lambda}} = \frac{\gamma_2}{\overline{\ell}|L|}(\overline{\ell}n_A\epsilon)^{2(1-\kappa)}C^{-2\lambda} \quad \text{at} \quad z = 0, \ -h, \quad (46)$$

where all quantities have to be taken with their respective index $\pm$ at the respective boundaries where the respective BCs apply. The full problem of energy and bandwidth is solved in section 6.

b. Relations of bandwidth, energy, and slope from Argo data

The power law Eq. (44) enables us to interpret the spectral parameters obtained from the Argo data in terms of the parametric model, in particular the data correlations shown in section 3. Our first attempt to use the full power law, i.e., the energy data ϵ together with the Brunt–Väisälä frequency dependent quantities $\overline{\ell}$ and C, failed completely to reproduce the E-sliced correlation in Fig. 2 (center panel). The dependence of $\overline{\ell}$ and C on the Brunt–Väisälä frequency, entering our model, reflects in the Argo-based data only the horizontal variations of N, which are substantial on the global scale of the analysis. Our parametric model and the resulting power law, on the other hand, are based on vertical propagation and vertical variations of N, which are not resolved in the Argo data that we used.

To this extent we abandon the explicit dependence on $\overline{\ell}$ and C and write Eq. (44) in logarithmic form

$$\log m_\star = \kappa(s)\log[n_A(s)\epsilon] + \gamma(s), \quad (47)$$

establishing a linear relation between the data $m_\star$ and $n_A\epsilon$ and the power-law exponent κ and an offset γ. These latter data are functions of the slope s. The question then is whether the model Eq. (47) reproduces the data correlations in section 3
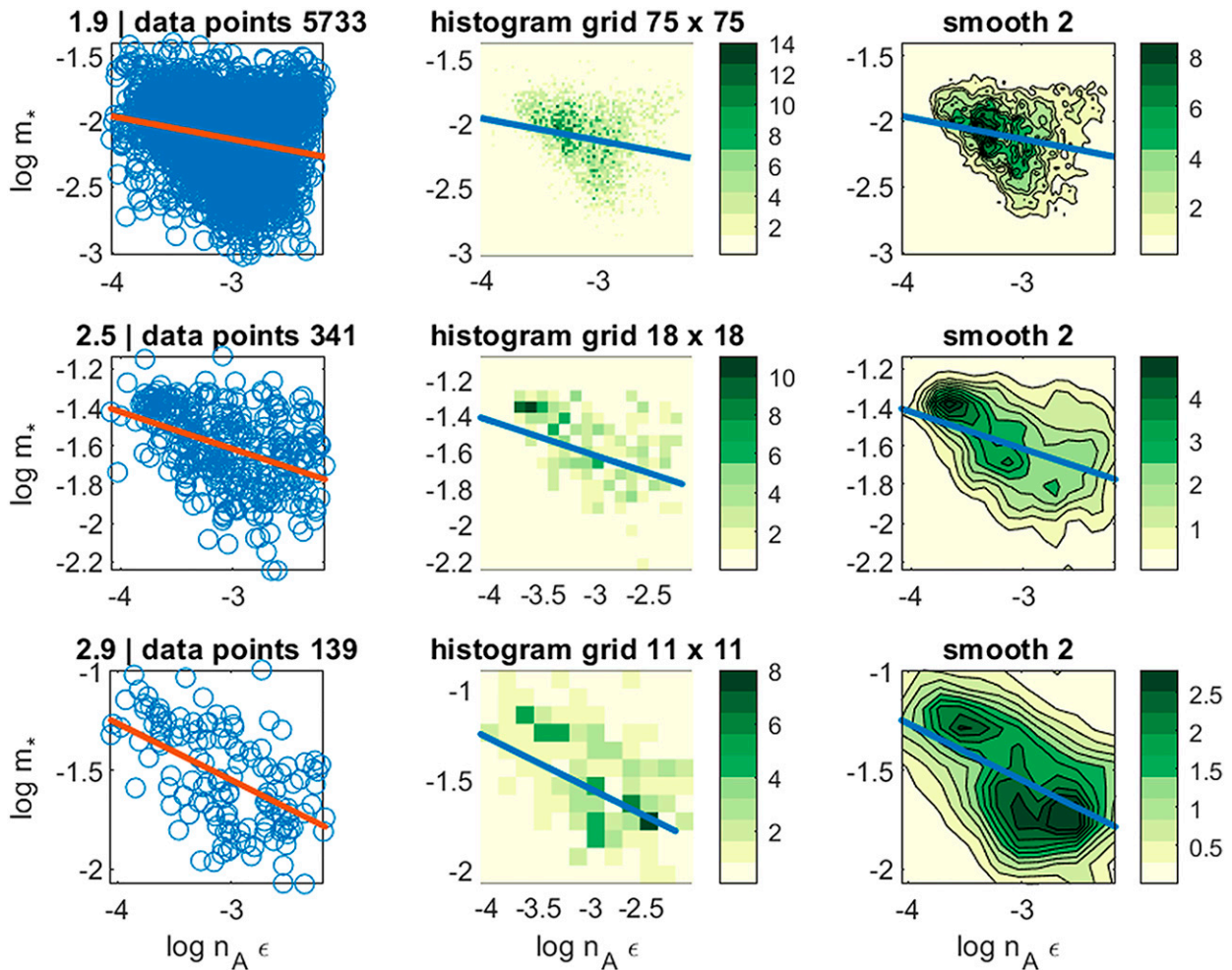
Fig. 4. (left) Scatterplots of the data $\log m_\star$ vs $\log n_A \varepsilon$ for the s-binned slicing. The bin values (lower limit of bin) are in the title of each panel. The red curves in each panel represent the fitted model Eq. (47). (center) Same data plotted as histograms. Grid intervals are equally spaced for the logarithmic values, the number of grid intervals is given in the title. (right) Smoothed version of the histogram data as contour plots. Data are from the depth range 300–500 m. The center and right plots contain the fitted linear regression (which is always performed with the scattered data in the left panel).

with a reasonable choice of the coefficient μ introduced in the previous section.

The data in Eq. (47) are meant for up and down waves but the fit performed by Pollmann (2020) to Argo-derived strain spectra does not distinguish between these wave branches. It resulted in estimates for the total energy of the GM spectrum and a mean wavenumber scale and a mean slope. We are bound to use these estimates as data in Eq. (47) and will thus not differentiate between up and down variables. Furthermore, the relation Eq. (47) should be valid in the whole water column but with the exception of a few recently introduced instruments not considered in the fits of Pollmann (2020) the Argo floats only cover the upper 2000 m of the ocean.

Our fitting procedure is then as follows: the coefficients κ and γ result from a least squares fit of the linear relation Eq. (47) to the Argo data of $m_\star$ and $n_A \varepsilon$, using data from all oceans but specific depth ranges (300–500 m, 500–1000 m, and

1000–2000 m). We concentrate on the fit for the 300–500-m depth range (results from the other depth ranges are similar but contain more noise; they are not shown here). For this to work the data $m_\star$ and $n_A \varepsilon$ are sliced (binned) into narrow ranges of slope s (we use bins of $\Delta s = 0.2$ for the slope range 1.6–4.2). The s-binned data are displayed in terms of scatterplots of $\log m_\star$ versus $\log n_A \varepsilon$ in Fig. 4 (left panels; together with the fit to be discussed below). The plots reflect the correlation envisioned in Fig. 2, showing a decrease of $\log m_\star$ with increasing modified energy $\log n_A \varepsilon$. Figure 5 shows the E-binned correlations in a similar slicing. In both cases the general pattern is masked by a substantial amount of noise.

There is an enormous change of the data number in the s bins: for low s values the number exceeds 10 000 points (for $s = 1.9$) while higher values are represented by much less data (of order 100 for $s = 2.9$). The scatter clouds for the low s values may thus hide correlation pattern that are not modeled
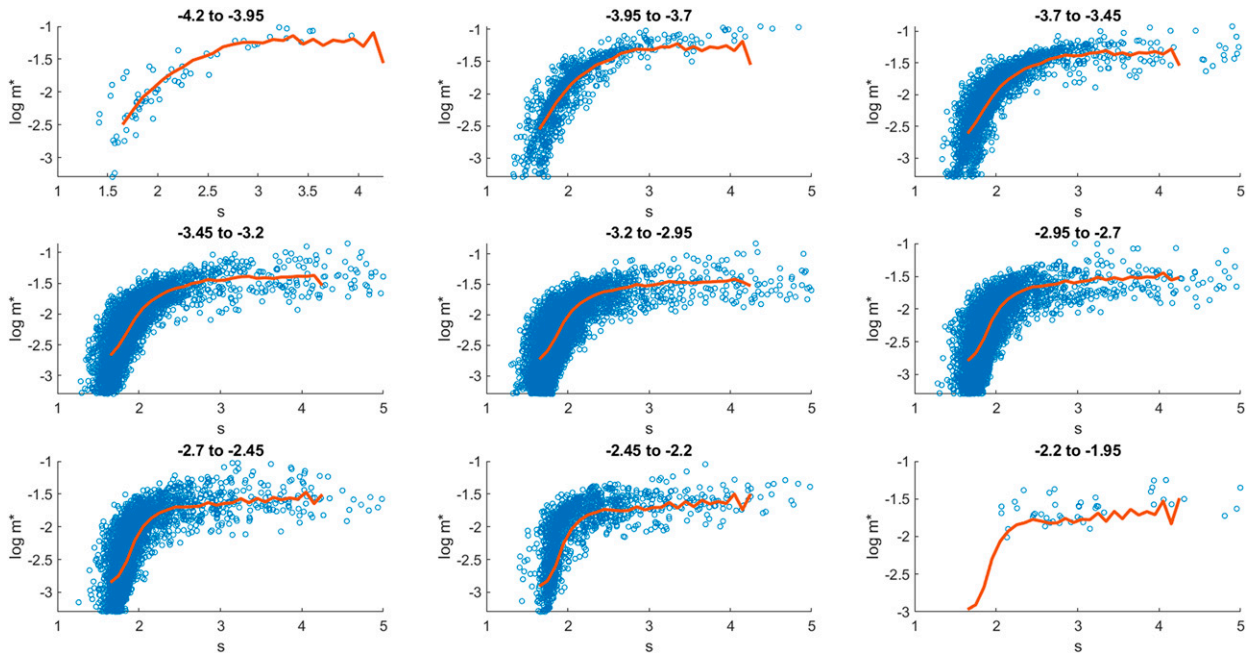
FIG. 5. Scatterplots of the data log$m_\star$ vs s for the E-binned slicing. The E-bin intervals are in the title of each panel. The red curves in each panel represent the fitted model Eq. (47). Data are from the depth range 300–500 m.

by the above linear regression. For this reason we show the data in two other versions, a histogram for sufficiently resolved grid, and a contour plot of smoothed histogram data. These are displayed in the center and right panels of Fig. 4. Only three cases of s bins are displayed, slopes are $s = 1.9$, 2.5, and 2.9. The histograms sometime reveal more than one concentration center, but the pattern generally supports the linear regression.

To establish the least squares form we add a noise term ϑ to the right-hand side of Eq. (47). We determine κ and γ by the least squares assumption $\langle \vartheta^2 \rangle = \min$. The least squares fit is made for each bin separately and estimates of $\kappa(s)$ and $\gamma(s)$ for the specific slice values of s are obtained. The result is shown in Fig. 6: we find negative κ for all slope values, almost constant and approximately -0.2. The associated parameter μ is very close to 1 (see bottom panel) in agreement with our assumptions. The fitted model is included with the red lines in the scatterplots Fig. 4 (left panels) for each separate s bin. In a corresponding way we plot the model in the E-binned scatterplots Fig. 5 (right panels), and the complicated correlation is reproduced successfully.

The large amount of noise in the Argo fits of $m_\star$ and ϵ deteriorates the fit of the model coefficients but does not prevent to extract the power-law properties. We have calculated the coefficient of determination R^2 (see, e.g., von Storch and Zwiers 1999) for the fit; see top panel of Fig. 6. It measures the extent to which the linear law on the right-hand side of the regression equation Eq. (47) (with the noise term added) determines the left-hand side. We found fairly low values of 0.1–0.3. This is the amount of variance explained by the fitted model (70%–90% is attributed to noise and only 10%–30%

to the linear model). The low values are, however, not an indication of model failure because the error pattern shows that there is no systematic deviation from the model. The top panel of Fig. 6 also displays the 95% confidence interval of the κ estimate, computed as described in von Storch and Zwiers (1999). In correspondence to the large scatter in the data the interval is quite large.

6. Numerical solutions of the energy–bandwidth equations

The problem of the scale and shape parameters of the internal wave spectrum is reduced to the functional Eq. (44), giving "bandwidth" in terms of energy by a power-law relation, to be implemented in the balance of energy Eq. (33). Replacing $m_\star$ by the steady-state power law of energy implies the notion that bandwidth adjusts faster than energy. But note that in practice solutions of Eq. (33) are required for coupling with an ocean model only in a floating quasi-steady state. The aim is to solve the set of equations Eqs. (33) and (44), extending the IDEMIX model of Olbers and Eden (2013) to nonconstant bandwidth. The equations are coupled and nonlinear in a complicated way: remember that $\Gamma^\pm$ depends on the boundary values of energies $\epsilon^\pm$; also the time scale τ_E depends on energy. There are two BCs at either of $z = -h$, 0 where energy fluxes are prescribed, as described above.

To achieve a numerical solution we follow the route described in the IDEMIX papers as, e.g., Olbers and Eden (2013). The energy balances for $\epsilon^\pm$ are reformulated to yield the balances for total energy $E = \epsilon^+ + \epsilon^-$ and energy asymmetry $\Delta = \epsilon^+ - \epsilon^-$. The latter is assumed steady, accounting
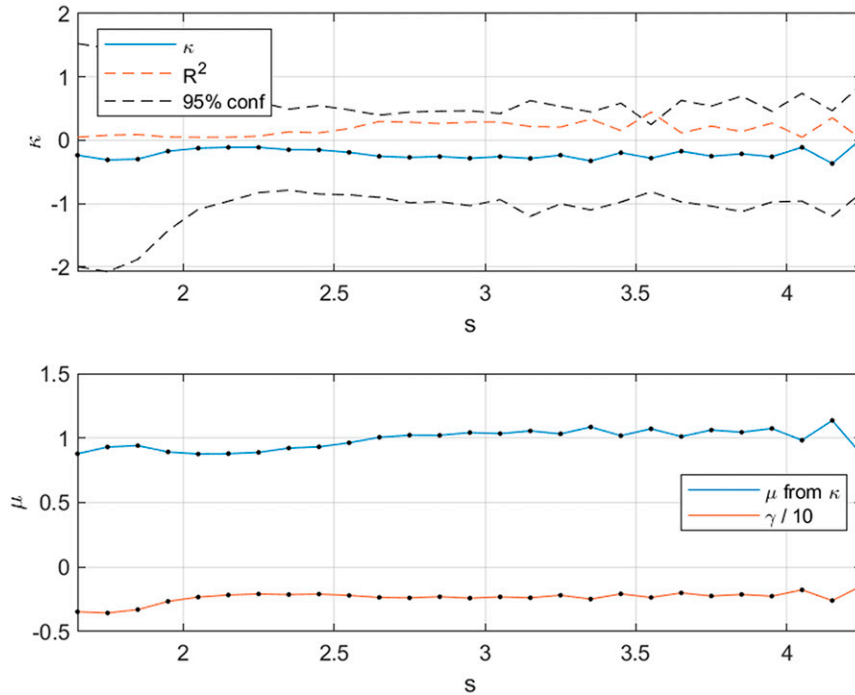
FIG. 6. The fitted coefficients κ and γ for the model Eq. (47) as function of the s-bin values. (top) Shown are κ (blue dotted), the coefficient of determination R^2 (red dashed), and the 95% confidence interval of the κ estimate (black dashed). (bottom) Shown are $\gamma/10$ (red dotted) and the value of μ (blue dotted) obtained from inverting the theoretical relation for κ given by Eq. (45).

for the heavy damping in the equation for Δ (see below). This enables us to reduce the two advective equations to a diffusion equation for E. We pursue this route, including turning point physics which has not been done before.

We use the energy balance Eq. (B7) with upstream turning point term for the turning point transfer, as described in appendix B,

$$\partial_t \epsilon + \sigma \partial_z \frac{\overline{\ell}\gamma\epsilon}{m_\star} + T_\epsilon = -\frac{1}{2}(\mu_0 E + \sigma\mu_1\Delta)\frac{1}{\tau_E}$$

$$T_\epsilon = -\sigma\alpha_\ell\left[H(N')\frac{\epsilon^-}{m_\star^-} - H(-N')\frac{\epsilon^+}{m_\star^+}\right] \quad (48)$$

with the abbreviations $\alpha_\ell = n_A \overline{n}|N'|$ and $\gamma = \gamma_1 n_A$. Taking sum and difference leads to the balance of total energy E and energy asymmetry Δ,

$$\partial_t E + \partial_z \overline{\ell}\gamma(\alpha E + \beta\Delta) = -\mu_0 \frac{E}{\tau_E},$$

$$\partial_t \Delta + \partial_z \overline{\ell}\gamma(\alpha\Delta + \beta E) + T_\epsilon^+ - T_\epsilon^- = -\mu_1 \frac{\Delta}{\tau_E}, \quad (49)$$

with

$$\alpha = \frac{1}{2}\frac{m_\star^- - m_\star^+}{m_\star^+ m_\star^-} \quad \text{and} \quad \beta = \frac{1}{2}\frac{m_\star^- + m_\star^+}{m_\star^+ m_\star^-}. \quad (50)$$

The turning point term becomes

$$T_\epsilon^+ - T_\epsilon^- = -2\alpha_\ell[\text{sign}(N')(\beta E + \alpha\Delta) - (\alpha E + \beta\Delta)]. \quad (51)$$

To proceed to the diffusive limit it is necessary to assume $\alpha\Delta \ll \beta E$, which is reasonable because α and Δ are both differences of positive quantities and β and E are the respective sums. Hence, we continue with

$$\partial_t \Delta + \partial_z(\overline{\ell}\gamma\beta E) - 2\alpha_\ell[\text{sign}(N')\beta E - \alpha E]$$

$$= -\left(\frac{\mu_1}{\tau_E} + 2\alpha_\ell\beta\right)\Delta = -\frac{\Delta}{\tau_1}. \quad (52)$$

Adjustment occurs with the time scale τ_1, which is small (of order 10 h for typical ocean conditions) compared to the time scale τ_E (a few days) of dissipation and nonlinear transfer. For times large compared to τ_1 the time tendency term in Eq. (52) can be neglected so that the balance of total energy becomes an advection–diffusion equation for total energy,

$$\partial_t E + \partial_z \overline{\ell}\gamma\alpha E + \partial_z\{\overline{\ell}\gamma\beta 2\tau_1\alpha_\ell[\text{sign}(N')\beta - \alpha]E\}$$

$$- \partial_z(\overline{\ell}\gamma\beta\tau_1\partial_z\overline{\ell}\gamma\beta E) = -\mu_0 \frac{E}{\tau_E}. \quad (53)$$

For the case of zero turning point transfer ($a_\ell = 0$) and fixed symmetric $m_\star$ the equation is that of the IDEMIX model of Olbers and Eden (2013). Here we show the behavior of Eq. (53), comparing the reference IDEMIX case with the solution for nonzero a_ℓ and with the varying bandwidth, given
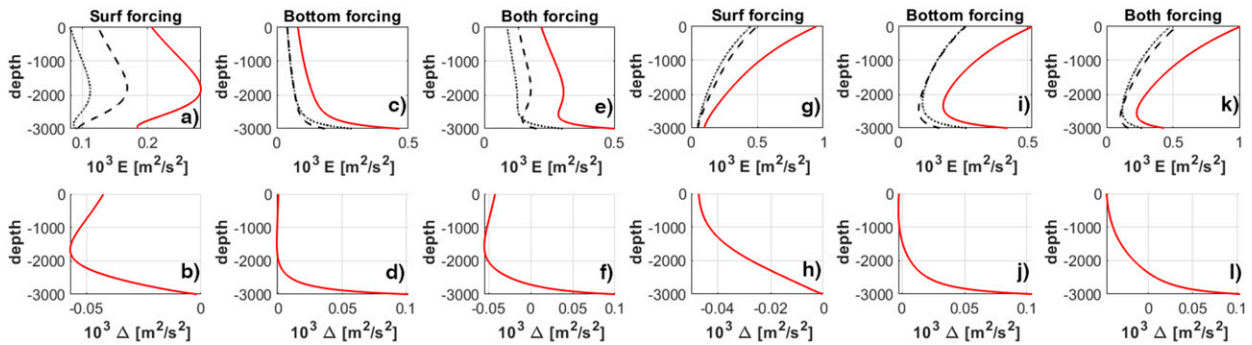
FIG. 7. (a)–(f) Reference case and (g)–(l) with turning point transfer active. Parameters are as described in the text. Surface, bottom, and both forcing functions are shown in the left, center, and right panels for each case group. (top) The total energy E (solid red) and the up–down energies ε^+ (dotted) and ε^- (dashed) at the end of the integration. (bottom) Energy asymmetry Δ. All energies are multiplied by the factor 10^3. The wavenumber scales $m_\star^+$ are held constant and equal in these cases.

by the power-law solution Eq. (44), which enters via the coefficients α and β. All solutions shown in the following have the same standard parameters: $\mu_0 = 1$, $\mu_1 = 5$, $\kappa = -0.1$, $\lambda = 0.1$; the forcing is $F_{\text{surf}} = -10^{-6}$ m^3 s^{-3}, $F_{\text{bot}} = 10^{-6}$ m^3 s^{-3} (switched on or off in the different experiments); the Brunt–Väisälä frequency profile is exponential $N(z) = N_0 e^{z/b}$ with $N_0 = 5.25 \times 10^{-3}$ s^{-1}, $b = 1300$ m, with an ocean depth of 3000 m, f is taken at 30° latitude. All solutions are for a slope $s = 2$ (dependence on the slope value is minor). The time scale τ_E is evaluated from Eq. (28) with a constant energy E and wavenumber scale $m_\star$ (GM values, see section 3) for the value entering τ_1 but with the actual E for the τ_E in the dissipation term. This way the model follows Olbers and Eden (2013) where the dissipation is quadratic in E but the damping coefficient of energy asymmetry Δ is independent of E.

The reference case (shown in Fig. 7) is similar but not identical to the simulations of the IDEMIX model of Olbers and Eden (2013). The parameters slightly differ and, in addition, the wavenumber scales $m_\star$ in those simulations were explicitly depth dependent [via $N(z)$] whereas here they are constant. The system comes to a steady state after roughly 10–20 days (due to damping by the τ_E time scale). The surface-forced case shows energies that increase from the surface to mid-depth and then strongly decrease with depth. With bottom forcing present E increases with depth in the whole water column and a deep minimum develops close to the bottom, significantly modifying the structure in the lower water column. It can be shown that these features arise due to the strong decrease of the Brunt–Väisälä frequency with depth (a constant N yields a parabolic decrease of E from the surface for surface forcing and from the bottom for bottom forcing, and a symmetric parabola for both forcing terms with a minimum at middepth; not shown). Note that the overall level of the energies is lower than the canonical GM value. This can be easily adjusted by increasing the forcing amplitude (see Fig. 8).

If turning point transfers are switched on (Figs. 7g–l) the simulations reveal an overall decrease of energies with depth right from the surface to the bottom. The values in the upper water column are increased. Bottom forcing modifies this structure with a deep minimum as in the previous reference

case. The approach to the steady state is faster due to the smaller time scale of the turning point physics (not shown).

If the bandwidth becomes predictive (see Fig. 8) by switching on the power-law formulation, the overall decrease of energies with depth is seen in all three simulations. The deep maximum is largely overwritten. The wavenumber scales (right panels) now change with depth: they are, however, almost constant in the vertical but differ significantly in their overall values in the three cases. For all forcing cases the scale $m_\star^-$ for downward waves exceeds the one $m_\star^+$ for upward waves. This feature is explained by the $N(z)$ profile decreasing with depth and its impact on the power-law amplitudes (for a "both forcing" case in a constant N profile up and down scales are identical, not shown). Also well documented is the increase of energy E with increasing forcing amplitude and the associated decrease of the wavenumber scales which, of course, is due to the power-law relation between bandwidth and energy.

7. Summary and conclusions

We have described a new member of the IDEMIX (Internal Wave Dissipation, Energy and Mixing) hierarchy of internal wave models which extends the energy prediction of the previous models to one of the most important spectral shape parameters: the bandwidth of the number of excited equivalent vertical modes. A closed set of equations predicting wave energy and bandwidth is derived by parametric projection of the complete energy balance equation (and boundary conditions) in phase space. This balance includes wave propagation and refraction in a prescribed stratification, nonlinear interactions, dissipation, and forcing by wind and tides. The coupled energy–bandwidth equations show the impact of all these processes, though, admittedly, in a simplified parametric way. Further, the present model is restricted to horizontally homogeneous conditions, but, as in all IDEMIX models, the model is viewed as a frame to host alternative or more complicated physical parameterizations of internal wave processes.

The model is formulated along the previous IDEMIX concept (see Olbers and Eden 2013), using energy compartments for up- and downward propagating waves, now equipped with
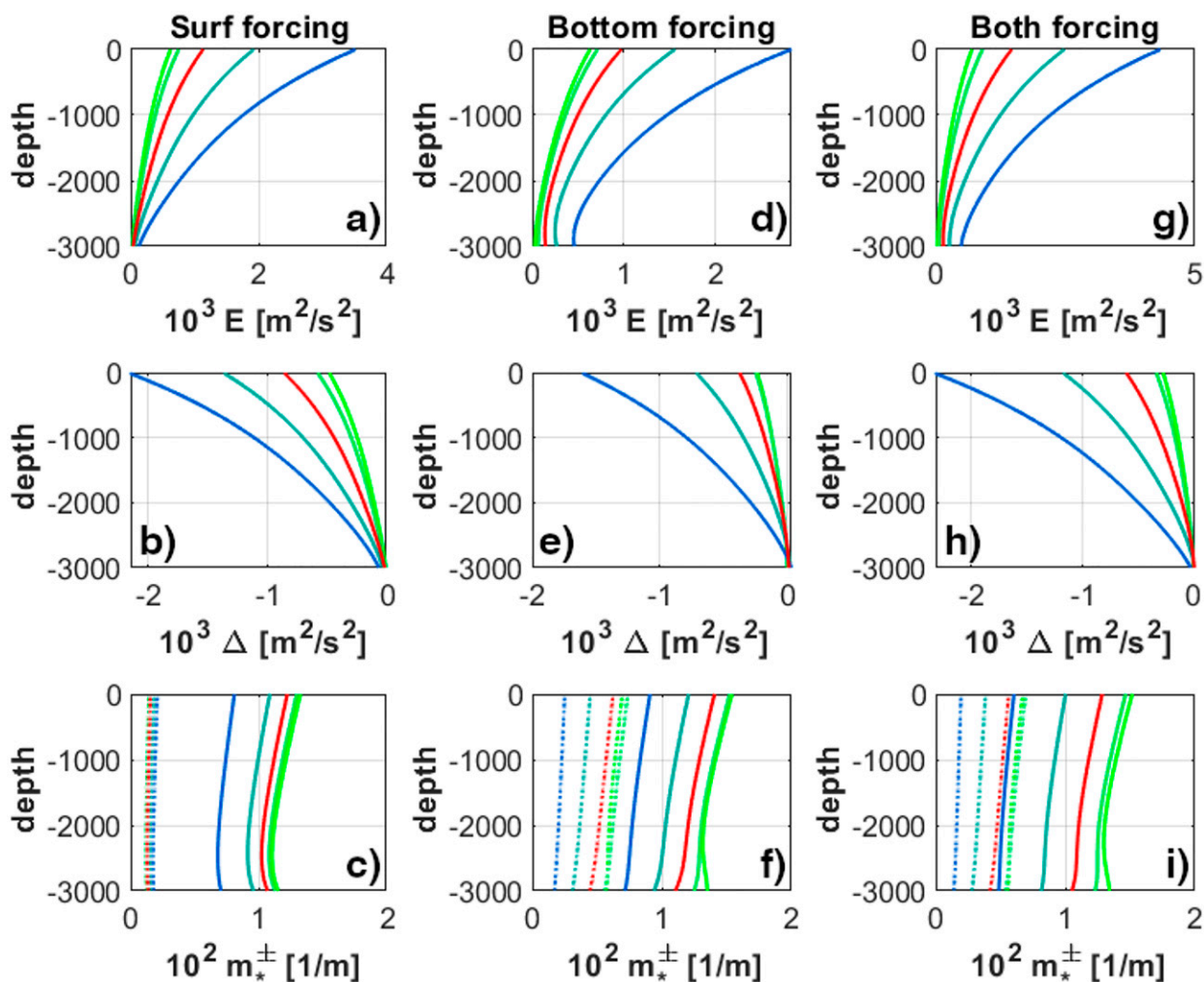
FIG. 8. As in Fig. 7, but with turning point transfer and power law active. The panels show E, Δ, and the wavenumbers scales $m_\star^\pm$ for five simulations with different forcing: the forcing at the bottom and the surface is multiplied by factors [0.1, 0.3, 1, 3, 10] (from blue to green, the standard case 1 has the color red). The bottom row shows $m_\star^+$ (dashed) and $m_\star^-$ (solid); the values are multiplied by 10^2.

the associated up and down bandwidth parameters. It thus consists of four coupled partial differential equations with boundary conditions at the ocean's top and bottom where there is energy inflow by wind and tidal forcing. In the present setup of the model these equations are formulated for energy compartments (up and down) and for a "squared" energy variable (also up and down), depending on bandwidth. Though an equation predicting bandwidth directly from the interplay of the above-mentioned processes can be readily derived, the setup in terms of "energy" compartments is preferred because boundary conditions are easily formulated from physical grounds for advective conservation equations in a more transparent way than for bandwidth.

The parametric projection uses a spectral model class of the energy distribution in wavenumber–frequency space as backbone, in our case the GM (Garrett–Munk) model class. Backbone means that the actual spectral state of the ocean wave field should be within reach of the model spectral class, i.e., it should be well approximated by specifying a set of model

parameters (in our case total energy and bandwidth). All projections result from suitably formulated integrations of the energy balance for this class. A number of model coefficients arises in these integrations, all of which represent well-defined integrals of the spectral model class: there are no tuning parameters, except that some of the coefficients are not precisely known because they arise from spectral properties that are largely unknown, as, e.g., spectral asymmetry.

A central question put to the model is what specific processes lead to specific values for the bandwidth. For the same question with respect to energy the answer is as expected: there is forcing of preferentially low modes by wind and/or baroclinic tides with a subsequent transfer by wave–wave interactions to high wavenumbers, where wave breaking and energy dissipation can be become effective. Because wave–wave interactions conserve energy in an integral way there is no immediate sign of this process in the balance of total energy in the IDEMIX models. The only impact of the process is

seen in the integrated vertical energy flux in physical space (the water column), which is partly set by damping of vertical asymmetries by nonlinear transfer in wavenumber space. Energy conservation of the nonlinear processes among waves is thus an important aspect of the IDEMIX models and it is quite easily implemented, avoiding any complicated parameterization.

But what sets the bandwidth? The answer is unspecific in a similar way: the bandwidth establishes its magnitude by the interplay of vertical propagation of the waves, structuring the vertical energy flux, and nonlinear transfer and dissipation, handling the spectral extent at high vertical wavenumbers. By simple reasoning with help of the balance equation of bandwidth (given in appendix C) we could indeed show that the wavenumber scale (bandwidth) of the GM class is largely given by three factors: a vertical stratification variable $\overline{\ell}$ (depending on the Coriolis frequency and Brunt–Väisälä frequency), a vertical scale b of the bandwidth flux, and the time scale τ_E of energy dissipation, resulting in

$$m_\star \simeq \frac{\overline{\ell}\tau_E}{b}. \qquad (54)$$

The relation may be rephrased as a matching of time scales: the time $bm_\star/\overline{\ell}$ of propagating energy perturbations by the vertical group velocity is thus of order of the dissipation time scale τ_E.

A more refined analysis reveals dependence on energy E, spectral slope s (in wavenumber space), and Brunt–Väisälä frequency N, and our further analytical treatment shows that $m_\star$ is given by a power-law relation in terms E and specific functions of s and N. This power-law relation is the most important result of our study. It is well confirmed by the parameter correlations among E, s, and $m_\star$, found in the Argo float data analysis of Pollmann (2020), and it can be used to extend previous IDEMIX models, in which $m_\star$ was taken constant, to a fully predictive mode in which energy and bandwidth are coupled and variable. These features of the study are well documented and discussed. A better representation of internal wave energetics and implied ocean mixing can thus be expected and is the topic of future investigations with the new parametric model. We intend to couple the energy–bandwidth model to a global ocean circulation model as done with previous IDEMIX models. We are also working to extend the model to include further shape parameters of the GM class, namely, the wavenumber slope, and to implement wave–mean flow interaction.

APPENDIX A

Coefficients

The coefficients arising from frequency averaging can be evaluated by analytical means. They are

$$\overline{\ell} = \frac{fn_B}{N^2 - f^2} \int_f^N \frac{\sqrt{\omega^2 - f^2}(N^2 - \omega^2)}{\omega^2} d\omega$$

$$= \frac{fn_B}{x^2 - 1}\left[\left(x^2 + \frac{1}{2}\right)\ln(x + \sqrt{x^2 - 1}) - \frac{3}{2}x\sqrt{x^2 - 1}\right],$$

$$\overline{n} = \frac{fNn_B}{N^2 - f^2} \int_f^N \frac{\sqrt{\omega^2 - f^2}}{\omega^2} d\omega$$

$$= \frac{n_B}{x^2 - 1}[x\ln(x + \sqrt{x^2 - 1}) - \sqrt{x^2 - 1}], \qquad (A1)$$

where $x = N/f$. The normalization of the frequency distribution is

$$n_B = \frac{2/\pi}{1 - 2/\pi\arcsin(f/N)}. \qquad (A2)$$

Note that f is here the modulus of the Coriolis frequency. The C function in Eq. (41) is given by

$$C/f^2 = \overline{\ell}/(fn_B)(x^2 - 1). \qquad (A3)$$

The s-dependent coefficients in the parametric model are

$$n_A(s) = \left(\int_{\lambda_\ell}^\infty \frac{1}{1 + \lambda^s}d\lambda\right)^{-1}, \quad \eta(s) = \left[\int_{\lambda_\ell}^\infty \frac{n_A^2(s)}{(1 + \lambda^s)^2}d\lambda\right]^{-1},$$

$$\gamma_1(s) = \int_{\lambda_\ell}^\infty \frac{1}{\lambda(1 + \lambda^s)}d\lambda, \quad \gamma_2(s) = 2\int_{\lambda_\ell}^\infty \frac{1}{\lambda(1 + \lambda^s)^2}d\lambda. \qquad (A4)$$

In all integrals we have extended the integration to infinite wavenumbers as an appropriate approximation. The coefficients n_A and η for zero cutoff, $\lambda_\ell = 0$, are

$$n_A(s) = \frac{s\sin\pi/s}{\pi} \quad \text{and} \quad \eta(s) = \frac{\pi}{(s - 1)\sin\pi/s}, \qquad (A5)$$

and we use these relations as sufficient approximations (correction to the above n_A expression is $-\lambda_\ell n_A^2 + \cdots$, which is small; similar for η). The coefficients γ_1 and γ_2 have no finite value for $\lambda_\ell = 0$, however, they can be expressed in terms of elementary functions

$$\gamma_1(s) = [(1/s)\ln(\lambda_\ell^s + 1) - \ln\lambda_\ell] \to -\ln\lambda_\ell, \qquad (A6)$$

$$\gamma_2(s) = -2\left\{(1/s)\left[\frac{1}{1 + \lambda_\ell^s} - \ln(\lambda_\ell^s + 1)\right] + \ln\lambda_\ell\right\}$$

$$\to -2[1/s + \ln\lambda_\ell], \qquad (A7)$$

where the indicated limits are for $\lambda_\ell \ll 1$. Then γ_1 becomes independent of s.

APPENDIX B

Evaluation of the Projections

The projected terms in the parameter equation Eq. (22) are

$$\Phi'_\epsilon(\tilde{A}/m) = -\sigma \int_{\lambda_\ell}^{\lambda_c} \tilde{A}/\lambda \, d\lambda,$$

$$\Phi'_\epsilon(\partial_m \tilde{A}) = -\sigma \tilde{A}(\lambda)|_{\lambda_\ell}^{\lambda_c}. \tag{B1}$$

Some of these expressions may be approximated: putting $\lambda_c = \infty$ in the integral and assuming $\lambda_\ell \sim 0.1 \ll 1$, $\lambda_c \gg 1$. Then

$$\Phi'_\epsilon(\tilde{A}/m) \simeq -\sigma n_A(s)\gamma_1$$

$$\Phi'_\epsilon(\partial_m \tilde{A}) \simeq \sigma n_A(s). \tag{B2}$$

The energy balance becomes

$$\partial_t \epsilon + \sigma \partial_z \frac{\overline{\ell}\gamma_1 n_A \epsilon}{m_\star} - \sigma n_A \frac{dN}{dz} \frac{\overline{n}\epsilon}{m_\star} = \Phi'_\epsilon(\hat{\mathcal{Q}}). \tag{B3}$$

The last term on the left-hand side describes turning point transfers. The present form, derived by straightforward integration of $\partial_m \tilde{A}$, does not satisfy conservation of total energy $\epsilon^+ + \epsilon^-$, which turning point physics should do. For this to work the integration must be done upstream. Consider for example a Brunt–Väisälä frequency profile such that $N' = dN/dz > 0$ in a certain depth range. Then part of the downward waves, with energy ϵ^-, gets reflected and the waves give their energy to upward waves with energy ϵ^+. Total energy is conserved in this process. Hence

$$\partial_t \epsilon^- + \ldots = -\alpha_\ell \epsilon^-/m_\star^-,$$

$$\partial_t \epsilon^+ + \ldots = \alpha_\ell \epsilon^-/m_\star^-, \tag{B4}$$

where $\alpha_\ell = \overline{n} n_A |N'|$. Similarly, if $N' < 0$, the upward energy is clipped and transfers that part to downward energy whereby

$$\partial_t \epsilon^+ + \ldots = -\alpha_\ell \epsilon^+/m_\star^+,$$

$$\partial_t \epsilon^- + \ldots = \alpha_\ell \epsilon^+/m_\star^+. \tag{B5}$$

With use of the Heaviside function H the equations are written as

$$\partial_t \epsilon^\pm + \ldots = \pm\alpha_\ell \left[H(N') \frac{\epsilon^-}{m_\star^-} - H(-N') \frac{\epsilon^+}{m_\star^+} \right], \tag{B6}$$

and the energy balance Eq. (B3) becomes

$$\partial_t \epsilon + \sigma \partial_z \frac{\overline{\ell}\gamma_1 n_A \epsilon}{m_\star} - \sigma n_A \overline{n} \left| \frac{dN}{dz} \right| \left[H(N') \frac{\epsilon^-}{m_\star^-} - H(-N') \frac{\epsilon^+}{m_\star^+} \right]$$

$$= \Phi'_\epsilon(\hat{\mathcal{Q}}). \tag{B7}$$

For the balance Eq. (25) of squared energy we find the terms

$$\Phi'_a\left(\partial_z \frac{\overline{\ell}\epsilon}{m_\star} \tilde{A}/m\right) = 2\frac{\epsilon}{m_\star} \int^\pm dm \tilde{A} \partial_z \left(\frac{\overline{\ell}\epsilon}{m_\star} \tilde{A}/m\right),$$

$$\Phi'_a(\partial_m \tilde{A}) = 2\frac{\epsilon}{m_\star} \int^\pm dm \tilde{A} \partial_m \tilde{A}, \tag{B8}$$

which lead to

$$\Phi'_a\left(\partial_z \frac{\overline{\ell}\epsilon}{m_\star} \tilde{A}/m\right) = -2\sigma \int_{\lambda_\ell}^{\lambda_c} \epsilon \tilde{A} \partial_z \frac{\overline{\ell}\epsilon}{m_\star^2} \tilde{A}/\lambda d\lambda,$$

$$\Phi'_a(\partial_m \tilde{A}) = -\sigma \frac{\epsilon}{m_\star} \tilde{A}^2(\lambda)\Big|_{\lambda_\ell}^{\lambda_c}. \tag{B9}$$

Also here the approximations are appropriate, hence

$$\Phi'_a\left(\partial_z \frac{\overline{\ell}\epsilon}{m_\star} \tilde{A}/m\right) = -\sigma n_A(s)\epsilon \partial_z \frac{\overline{\ell}\gamma_2 n_A(s)\epsilon}{m_\star^2}$$

$$\Phi'_a(\partial_m \tilde{A}) \simeq \sigma \frac{\epsilon}{m_\star} n_A^2(s). \tag{B10}$$

In Eq. (B10) we have neglected a term $\sim\partial_z s$ arising from interchanging $1/(1 + \lambda^s)$ with the derivative ∂_z. The squared energy balance then becomes

$$\partial_t a + \sigma n_A \epsilon \partial_z \frac{\overline{\ell}\gamma_2 n_A \epsilon}{m_\star^2} - \sigma n_A^2 \frac{dN}{dz} \frac{\overline{n}\epsilon^2}{m_\star^2} = \Phi'_a(\hat{\mathcal{Q}}). \tag{B11}$$

The integrals γ_1 and γ_2 can be reduced logarithmic expressions which can be approximated to simple expressions (see appendix A).

For the turning point term in Eq. (B11) the same argument applies as for the energy balance, hence with the upstream form,

$$\partial_t a + \sigma n_A \epsilon \partial_z \frac{\overline{\ell}\gamma_2 n_A \epsilon}{m_\star^2} - \sigma n_A^2 \overline{n} \left| \frac{dN}{dz} \right|$$

$$\times \left[H(N') \frac{(\epsilon^-)^2}{(m_\star^-)^2} - H(-N') \frac{(\epsilon^+)^2}{(m_\star^+)^2} \right] = \Phi'_a(\hat{\mathcal{Q}}). \tag{B12}$$

APPENDIX C

The Bandwidth Balance

An equation directly determining $m_\star$ can be derived from Eqs. (33) and (34) by elimination of $\partial_t \epsilon$. This yields

$$\partial_t m_\star - \sigma \frac{\eta m_\star^2}{\epsilon} n_A \partial_z \left(\frac{\overline{\ell}\gamma_2 n_A \epsilon}{m_\star^2}\right) + 2\sigma \frac{m_\star}{\epsilon} \partial_z \left(\frac{\overline{\ell}\gamma_1 n_A \epsilon}{m_\star}\right) + T = W, \tag{C1}$$

with

$$W = -\frac{m_\star}{\epsilon} [(\mu_0 - \eta\mu_2)E + \sigma(\mu_1 - \eta\mu_3)\Delta] \frac{1}{\tau_E},$$

$$T = -\frac{\eta m_\star^2}{\epsilon^2} T_a + 2\frac{m_\star}{\epsilon} T_\epsilon = \sigma \frac{dN}{dz} \overline{n} n_A(\eta n_A - 1), \tag{C2}$$

taking in T for simplicity the nonconserving form of the turning point transfers. All divergences and the T term can

be converted to a logarithmic expression for the flux. One finds

$$\partial_t\left(\frac{m_\star}{\overline{\ell}n_A}\right) + \sigma\,\partial_z\ln[(\overline{\ell}n_A\epsilon)^{2\gamma_1-\eta n_A\gamma_2}(m_\star^2)^{-\gamma_1+\eta n_A\gamma_2}C^{(\eta n_A-1)/2}] = \frac{W}{\overline{\ell}n_A}.$$
(C3)

Contrary to the squared energy variable, the quantity $m_\star/\overline{\ell}n_A$ thus satisfies a conservative balance, with a source term from wave dissipation and asymmetry damping. $m_\star/\overline{\ell}n_A$ can be viewed as an inverse mean group velocity. The source term W, given by Eq. (C2), in the balance of bandwidth reveals interesting properties: the contribution from energy dissipation (the $\mu_0 E$ term) leads to a damping of bandwidth, the time scale of this process is τ_E/μ_0. This feature is to be expected because dissipation shrinks the energy spectrum at high wavenumbers and reduces the bandwidth. The contribution from squared energy, on the other hand, the $\mu_2 E$ term is a source, increasing bandwidth with a time scale $\tau_E/(\eta\mu_2)$. With $\mu_2 \sim \mu_0$ and $\eta \simeq \pi$, the net W term likely represents a source that must be balanced by the flux divergence.

A rough estimate of the magnitude of the bandwidth for our model can be obtained from Eq. (C3): since the divergence of the logarithmic flux is simply an (inverse) vertical scale, say b, we arrive at $(m_\star/\overline{\ell}n_A) \simeq \tau_E/(\mu_0 b)$. The time of propagating energy perturbations in the vertical is thus of order of the dissipation time scale.

REFERENCES

Alford, M. H., J. A. MacKinnon, H. L. Simmons, and J. D. Nash, 2016: Near-inertial internal gravity waves in the ocean. *Annu. Rev. Mar. Sci.*, **8**, 95–123, https://doi.org/10.1146/annurev-marine-010814-015746.

Bell, T. H., Jr., 1975: Topographically generated internal waves in the open ocean. *J. Geophys. Res.*, **80**, 320–327, https://doi.org/10.1029/JC080i003p00320.

Cairns, J. L., and G. O. Williams, 1976: Internal wave observations from a midwater float, 2. *J. Geophys. Res.*, **81**, 1943–1950, https://doi.org/10.1029/JC081i012p01943.

Eden, C., and D. Olbers, 2014: An energy compartment model for propagation, non-linear interaction and dissipation of internal gravity waves. *J. Phys. Oceanogr.*, **44**, 2093–2106, https://doi.org/10.1175/JPO-D-13-0224.1.

——, F. Pollmann, and D. Olbers, 2019: Numerical evaluation of energy transfers in internal gravity wave spectra of the ocean. *J. Phys. Oceanogr.*, **49**, 737–749, https://doi.org/10.1175/JPO-D-18-0075.1.

Eriksen, C. C., 1982: Observations of internal wave reflection off sloping bottoms. *J. Geophys. Res.*, **87**, 525–538, https://doi.org/10.1029/JC087iC01p00525.

Garrett, C., and W. Munk, 1972: Space-time scales of internal waves. *Geophys. Fluid Dyn.*, **3**, 225–264, https://doi.org/10.1080/03091927208236082.

——, and ——, 1975: Space-time scales of internal waves: A progress report. *J. Geophys. Res.*, **80**, 291–297, https://doi.org/10.1029/JC080i003p00291.

——, and E. Kunze, 2007: Internal tide generation in the deep ocean. *Annu. Rev. Fluid Mech.*, **39**, 57–87, https://doi.org/10.1146/annurev.fluid.39.050905.110227.

Gregg, M. C., 1989: Scaling turbulent dissipation in the thermocline. *J. Geophys. Res.*, **94**, 9686–9698, https://doi.org/10.1029/JC094iC07p09686.

Hasselmann, K., 1968: Weak-interaction theory of ocean waves. *Basic Dev. Fluid Dyn.*, **2**, 117–182, https://doi.org/10.1016/B978-0-12-395520-3.50008-6.

——, and Coauthors, 1973: Measurements of wind-wave growth and swell decay during the joint North Sea wave project (JONSWAP). *Dtsch. Hydrogr. Z.*, **12**, 1–95.

——, W. Sell, D. B. Ross, and P. Müller, 1976: A parametric wave prediction model. *J. Phys. Oceanogr.*, **6**, 200–228, https://doi.org/10.1175/1520-0485(1976)006<0200:APWPM>2.0.CO;2.

Kunze, E., E. Firing, J. M. Hummon, T. K. Chereskin, and A. M. Thurnherr, 2006: Global abyssal mixing inferred from lowered ADCP shear and CTD strain profiles. *J. Phys. Oceanogr.*, **36**, 1553–1576, https://doi.org/10.1175/JPO2926.1.

Le Boyer, A., and M. H. Alford, 2021: Variability and sources of the internal wave continuum examined from global moored velocity records. *J. Phys. Oceanogr.*, **51**, 2807–2823, https://doi.org/10.1175/JPO-D-20-0155.1.

Levine, M. D., 2002: A modification of the Garrett–Munk internal wave spectrum. *J. Phys. Oceanogr.*, **32**, 3166–3181, https://doi.org/10.1175/1520-0485(2002)032<3166:AMOTGM>2.0.CO;2.

Müller, P., D. Olbers, and J. Willebrand, 1978: The IWEX spectrum. *J. Geophys. Res.*, **83**, 479–500, https://doi.org/10.1029/JC083iC01p00479.

——, G. Holloway, F. Henyey, and N. Pomphrey, 1986: Nonlinear interactions among internal gravity waves. *Rev. Geophys.*, **24**, 493–536, https://doi.org/10.1029/RG024i003p00493.

Munk, W., 1981: Internal waves and small-scale processes. *Evolution of Physical Oceanography*, B. A. Warren and C. Wunsch, Eds., MIT Press, 264–291.

Olbers, D., 1986: Internal gravity waves. *Landolt-Börnstein*, J. Sündermann, Ed., Numerical Data and Functional Relationships in Science and Technology-New Series, Group V, Vol. 3a, Springer, 37–82.

——, and C. Eden, 2013: A global model for the diapycnal diffusivity induced by internal gravity waves. *J. Phys. Oceanogr.*, **43**, 1759–1779, https://doi.org/10.1175/JPO-D-12-0207.1.

——, P. Jurgenowski, and C. Eden, 2020a: A wind-driven model of the ocean surface layer with wave radiation physics. *Ocean Dyn.*, **70**, 1067–1088, https://doi.org/10.1007/s10236-020-01376-2.

——, F. Pollmann, and C. Eden, 2020b: On PSI interactions in internal gravity wave fields and the decay of baroclinic tides. *J. Phys. Oceanogr.*, **50**, 751–771, https://doi.org/10.1175/JPO-D-19-0224.1.

Olbers, D. J., 1976: Nonlinear energy transfer and the energy balance of the internal wave field in the deep ocean. *J. Fluid Mech.*, **74**, 375–399, https://doi.org/10.1017/S0022112076001857.

——, 1983: Models of the oceanic internal wave field. *Rev. Geophys.*, **21**, 1567–1606, https://doi.org/10.1029/RG021i007p01567.

Pollmann, F., 2020: Global characterization of the ocean's internal wave spectrum. *J. Phys. Oceanogr.*, **50**, 1871–1891, https://doi.org/10.1175/JPO-D-19-0185.1.

——, 2022: Global characterization of the ocean's internal gravity wave vertical wavenumber spectrum from Argo float profiles. Zenodo, accessed 7 May 2023, https://doi.org/10.5281/zenodo.6966416.

——, C. Eden, and D. Olbers, 2017: Evaluating the global internal wave model IDEMIX using finestructure methods. *J. Phys.*

Oceanogr., **47**, 2267–2289, https://doi.org/10.1175/JPO-D-16-0204.1.

Polzin, K. L., and Y. V. Lvov, 2011: Toward regional characterizations of the oceanic internal wavefield. *Rev. Geophys.*, **49**, RG4003, https://doi.org/10.1029/2010RG000329.

——, A. C. Naveira Garabato, T. N. Huussen, B. M. Sloyan, and S. Waterman, 2014: Finescale parameterizations of turbulent dissipation. *J. Geophys. Res. Oceans*, **119**, 1383–1419, https://doi.org/10.1002/2013JC008979.

Riser, S. C., and Coauthors, 2016: Fifteen years of ocean observations with the global Argo array. *Nat. Climate Change*, **6**, 145–153, https://doi.org/10.1038/nclimate2872.

von Storch, H., and F. W. Zwiers, 1999: *Statistical Analysis in Climate Research*. Cambridge University Press, 503 pp.

Whalen, C. B., L. D. Talley, and J. A. MacKinnon, 2012: Spatial and temporal variability of global ocean mixing inferred from Argo profiles. *Geophys. Res. Lett.*, **39**, L18612, https://doi.org/10.1029/2012GL053196.